NONLINEAR CONTROLLER DESIGN FOR HIGH SPEED DYNAMIC ATOMIC FORCE MICROSCOPE SYSTEM

A Thesis Submitted to
the Graduate School of Engineering and Sciences of
İzmir Institute of Technology
in Partial Fulfillment of the Requirements for the Degree of

MASTER OF SCIENCE

in Electronics and Communication Engineering

by
Alper COŞAR

December 2018
İZMİR

We approve the thesis of **Alper COŞAR**

Examining Committee Members:

Assoc. Prof. Dr. Müjdat BALANTEKİN
Department of Electrical and Electronics Engineering
İzmir Institute of Technology

Assist. Prof. Dr. Hatice DOĞAN
Department of Electrical and Electronics Engineering
Dokuz Eylül University

Assist. Prof. Dr. Barbaros ÖZDEMİREL
Department of Electrical and Electronics Engineering
İzmir Institute of Technology

25 December 2018

Assoc. Prof. Dr. Müjdat BALANTEKİN
Supervisor, Department of Electrical and Electronics Engineering
İzmir Institute of Technology

Prof. Dr. Enver TATLICIOĞLU
Head of the Department of
Electrical and Electronics Engineering

Prof. Dr. Aysun SOFUOĞLU
Dean of the Graduate School of
Engineering and Sciences

ACKNOWLEDGMENTS

First of all, I would like to express my deep gratitude to my advisor Assoc. Prof. Dr. Müjdat BALANTEKİN for his understanding, guidance, encouragement and incredible support in every stage of my thesis study.

I would like to express my sincere thanks to Prof. Dr. Gildas BESANÇON and Dr. Alina VODA for their support and guidance during my internship in GIPSA-LAB, Grenoble, FRANCE during October 2017/January 2018, which is related to improvement of the AFM-like Scanning-Tunneling Microscope (STM) platform and provided me a great experience for understanding the operation and key features of such tools.

I would like to thank committee members, Assist. Prof. Dr. Hatice DOĞAN and Assist. Prof. Dr. Barbaros ÖZDEMİREL, for giving me contribution which helped me a lot in revising the thesis.

Finally, I would like to thank my parents, and my sister for their unconditional and endless support.

ABSTRACT

NONLINEAR CONTROLLER DESIGN FOR HIGH SPEED DYNAMIC ATOMIC FORCE MICROSCOPE SYSTEM

In this study, the performances of conventionally used PI controller and a nonlinear H_∞ controller, are compared in the state-of-the-art High-Speed Dynamic Atomic Force Microscope (HS-AFM). The state-of-the-art HS-AFM system is modeled via MATLAB/SIMULINK for four different cantilevers, i.e., small high-frequency and regular low-frequency cantilevers used in air and liquid environments. For the modeled system, PI and H_∞ controllers are designed and implemented by using both analytical methods and toolboxes available in MATLAB. Simulations are performed in ideal condition, and under exogenous effects such as noise, disturbance and parametric uncertainty. In ideal condition, achieved maximum frame rate, and the percentage of topography acquisition error with two controllers are calculated for each cantilever. Also, performances of controllers in the system are tested under exogenous effects. It is observed that with the H_∞ controller, the topography of the selected sample can be obtained with up to 2 times less acquisition error. It is also observed that PI controller is better in disturbance rejection, but H_∞ controller is more robust under the effect of noise. For each cantilever, similar results to the ideal condition is obtained in case of uncertainty. Most distinctive results are obtained with high-frequency cantilevers, as H_∞ controller enables a 2 times higher frame rate (14.3 fps) compared to the PI controller (7.1 fps) with the same level of acquisition error in the state-of-the-art HS-AFM operated in liquid environment.

ÖZET

YÜKSEK HIZLI DİNAMİK ATOMİK KUVVET MİKROSKOBU SİSTEMİ İÇİN DOĞRUSAL OLMAYAN DENETÇİ TASARIMI

Bu çalışmada, en gelişkin Yüksek Hızlı Dinamik Atomik Kuvvet Mikroskobu (YH-AKM) sisteminde geleneksel olarak kullanılan PI kontrolcüsü ile bir doğrusal olmayan H_∞ kontrolcüsünün performansları kıyaslanmıştır. En gelişkin YH-AKM sistemi MATLAB/SIMULINK'de, hava ve sıvıda küçük yüksek-frekanslı ve sıradan düşük-frekanslı olmak üzere dört farklı prob için modellenmiştir. Modellenen sistem için, PI ve H_∞ kontrolcüleri analitik metodlar ve MATLAB'daki araçlar kullanılarak tasarlanıp gerçekleştirilmiştir. Simülasyonlar hem ideal koşulda, hem de gürültü, parazit ve parametrik belirsizlik gibi dış etkiler ile gerçekleştirilmiştir. İdeal koşulda, ulaşılan maksimum çerçeve hızı ve yüzdelik topografi yakalama hatası iki kontrolcü ile her prob için hesaplanmıştır. Ayrıca, dış etkilere karşı kontrolcülerin sistemdeki performansları test edilmiştir. H_∞ kontrolcüsü ile, seçilen örneğin topografisinin 2 kata kadar daha az yakalama hatası ile elde edilebildiği görülmüştür. Ayrıca PI kontrolcüsünün bozunum reddinde daha iyi, fakat H_∞ kontrolcüsünün gürültü etkisi altında daha sağlam olduğu gözlemlenmiştir. Her prob için, belirsizlik durumunda ideal koşula benzer sonuçlar elde edilmiştir. En belirgin sonuçlar yüksek-frekanslı problarla elde edilmiştir, çünkü H_∞ kontrolcüsü sıvıda çalıştırılan son teknoloji YH-AKM'de, aynı yakalama hatası ile PI kontrolcüsüne (7.1 fps) oranla 2 kat daha yüksek çerçeve hızına (14.3 fps) imkan vermektedir.

TABLE OF CONTENTS

LIST OF FIGURES

LIST OF TABLES

Table **Page**

LIST OF ABBREVIATIONS

AFM . . . . . Atomic Force Microscope
HS-AFM . . . . . High Speed Atomic Force Microscope
AM-AFM . . . . . Amplitude-Modulation Atomic Force Microscope
FM-AFM . . . . . Frequency-Modulation Atomic Force Microscope
SEM . . . . . Scanning Electron Microscope
MIMO . . . . . Multi-Input Multi-Output
SISO . . . . . Single-Input Single-Output
MEMS . . . . . Micro Electro-Mechanical Systems
PID . . . . . Proportional-Integral-Derivative
PI . . . . . Proportional-Integral
PD . . . . . Proportional-Derivative
H_∞ . . . . . H-infinity
OBD . . . . . Optical Beam Deflection
DC . . . . . Direct Current
UHV . . . . . Ultra High-Vacuum
DNA . . . . . Deoxyribo Nucleic Acid
RNA . . . . . Ribo Nucleic Acid
MHz . . . . . Mega-Hertz
kHz . . . . . kilo-Hertz
N/m . . . . . Newton per meter
fps . . . . . frames per second
nm . . . . . nanometer
DMT . . . . . Derjaguin-Müller-Toporov
GPa . . . . . Giga-Pascal
ODE . . . . . Ordinary Differential Equation
dB . . . . . Decibel
ms . . . . . miliseconds
μ_s . . . . . microseconds
rad/s . . . . . radians per second
FPGA . . . . . Field Programmable Gate Array
rms . . . . . root mean square

CHAPTER 1

INTRODUCTION

Atomic Force Microscope (AFM) (Binnig et al., 1986) is a type of scanning-probe microscope that allows one to visualize the surface features of a sample material or an object in nano-scale by scanning its surface with a probe, which is called as cantilever beam. Additionally, it can be used to investigate the substantial properties of a material, such as its elasticity, conductivity, etc. The High-Speed AFM (HS-AFM), which provides the main motivation for this study, is the advanced type of AFM, which enables scanning the material in high scan rates. Due to its high speed, HS-AFM enables observing dynamic processes in nano-scale related to biology, nanoscience and material sciences, which occur in a very short time. Thus, it has an increasing popularity in those disciplines.

In this thesis, the effect of two controller design approaches that are PI controller design, which is preferred in commercial AFM and the state-of-the-art HS-AFM, and Robust H_∞ controller, which is proposed to improve the scan speed of HS-AFM in numerous studies in the literature, are compared. Robust H_∞ control is a nonlinear controller design method that is used in various systems in daily life, such as DC Motor (Brezina and Brezina, 2011), vehicles (Rigatos et al., 2015; Mahapatra and Subudhi, 2017), robots (Oubellil et al., 2016), balance systems (Rigatos et al., 2017) and other types of systems (Zhang et al., 2018). Additionally, as mentioned, there are many studies in the literature that are dedicated to perform the Robust H_∞ control on AFM and HS-AFM (Peng et al., 2015; Chuang et al., 2013; Schitter et al., 2001; Nakakuki et al., 2012). They mainly focus on improving the scan rate of the HS-AFM, and enhancing the robustness of the system. Most of them are carried out in real-time systems, and controllers are found via analytical methods. Results of these studies have shown that the scan rate can be increased further with H_∞ controller in comparison to the PI controller.

The state-of-the-art HS-AFM system is modeled in MATLAB/SIMULINK environment in this study. In this way, its dynamics are reflected in the simulator. In the model generated for the state-of-the-art HS-AFM, four different cantilevers are used. These are two regular low-frequency cantilevers that are preferred in commercial AFM systems, and two small high-frequency cantilevers that are preferred in the state-of-the-art HS-AFM utilized in air and liquid environments. The system model generated in this study has four versions, and controller designs are made for these four cases as the system

dynamics change with each cantilever used. Once the system model is generated with these cantilevers, PI and H_∞ controllers are designed for each cantilever by using both analytical methods and toolboxes available in MATLAB. Simulations are performed, and performances of these controllers are compared in terms of their accuracy in surface topography acquisition, minimum time required for them to acquire the topography with allowed percentage error, and maximum frame rate achieved with these controllers for each cantilever. Furthermore, performances of these controllers are compared under the effect of noise, disturbance and parametric uncertainty. Thus, not only the achieved scan rate and accuracy of obtained topography with these controllers are found, but also the robustness of controllers in response to exogenous effects are tested.

Previous studies in the literature are performed for a single cantilever, which tends to be a regular cantilever for the studies in commercial AFM and small cantilever for the ones in HS-AFM. Thus, this thesis provides a new perspective for the studies to observe the effect of H_∞ controller design in HS-AFM in the literature, since it investigates the performances of typically used PI controller and widely proposed H_∞ controller not only for a small high-frequency cantilever, but also for four different cantilevers including both regular cantilevers and small cantilevers in the modeled state-of-the-art HS-AFM operated in both air and liquid environments.

In Chapter 2, working principle of a commercial AFM is briefly explained. The structure of the cantilever beam, which is used as the scanning probe of the AFM and HS-AFM is given. Types of AFM are explained in terms of driving and detection methods. Then, efforts that are dedicated to improve the scan speed of commercial AFM, in order to obtain HS-AFM are given. Finally, the structure of the state-of-the-art HS-AFM that is developed by Ando (Ando, 2012), which constitutes the system of interest for this study, is given. In Chapter 3, structure of the state-of-the-art HS-AFM model generated via MATLAB/SIMULINK in this study is explained element-by-element. Mathematical models of the working principles of these elements, and methods of modeling them in SIMULINK environment are given.

In Chapter 4, PI and H_∞ controller design methods, which are used to obtain the controller for the modeled state-of-the-art HS-AFM in this study, are briefly explained. Criteria for choosing their parameters are given. Finally, the false error method used as an auxiliary tool to both PI and H_∞ controllers, to overcome the error signal saturation problem, is explained. Again, values of the parameters used in false error generation, and the criterion of choosing them is explained.

In Chapter 5, simulation results obtained with PI and H_∞ controllers for each cantilever is given and discussed. Minimum acquisition time, the error between the actual topography and the acquired topography, and the frame rate obtained with these controllers for each cantilever are given. Frequency responses of both the closed-loop sensitivity functions, and transfer functions from the error signal to the actuator signal are obtained. Simulations in ideal conditions, and with noise, disturbance and parametric uncertainty are performed. In the obtained results, the actual sample topography, and controller responses that represent the acquired topography with these controllers are shown together in the same scale. Results are discussed with the help of frequency response of closed-loop sensitivity functions and the bode diagrams of the actuator response.

In the final chapter, results obtained from this thesis are summarized. How this study can be further advanced, and other possible control methods that can be proposed for the modeled state-of-the-art HS-AFM system in this study, are discussed.

CHAPTER 2

THE HIGH-SPEED DYNAMIC ATOMIC FORCE MICROSCOPE

2.1. General Structure of the AFM

After its invention in early 1980s, AFM has contributed a lot to the various scientific disciplines such as nanometrics, material science, molecular biology, etc. that require observations in atomic or molecular scale. Since it plays a very important role in those disciplines, numerous works has been conducted to improve the AFM system after its invention, and several types of AFM having state-of-the-art components and different working principles have been arisen. In this chapter, the general structure and different types of the AFM, together with studies dedicated to improvement of the AFM towards the High-Speed AFM (HS-AFM), and Ando's HS-AFM system (Ando, 2012) that is used in this study are explained.

Monitoring a sample in AFM is done by scanning the sample material with a probe, which is called as the cantilever beam. The cantilever is generally a micro-fabricated, rectangular-shaped beam that has a conical or pyramidal sharp tip at its free-end. It is connected to a holder through its fixed-end. Some cantilevers used in special applications (e.g. mass detection) does not have this sharp tip at the end, and are not necessarily in a rectangular shape. The sharp tip generally has a diameter of few nanometers, but it varies in fabrication according to the utilization purpose along with the total size of the cantilever. Mechanical properties of the cantilever, i.e., its spring constant, quality factor, and resonance frequency depend on the size, material used for manufacturing it, and the operating environment. Small cantilevers have high resonance frequencies, while regular cantilevers large in size tend to have low resonance frequencies. Additionally, cantilevers manufactured for applications in air tend to be stiff, i.e., their spring constants are high. For sensitive materials, such as biological samples, scan is done in liquid and cantilevers used to scan these materials have very low spring constants (generally lower than 1 N/m).

During the scan in AFM, the sample (or in some types of AFM, the cantilever) is moved along the line in x-axis, and the tip starts to trace the sample surface. When

the scan of a line in x-axis on the sample surface finishes, the sample (or the cantilever) is skipped by a single line in y-axis so that the tip starts to trace a new line in x-axis. This is done via X-Y scanner piezos. Cantilever deflects in vertical z-axis when there is a change in topography, i.e., the tip faces a peak or a hollow on the sample surface while tracing it. This deflection is caused by interaction forces arising between the tip and the sample. Deflection rate is detected by a sensor and used for Z-feedback control, which serves to prevent a detrimental tip-sample interaction during the scan. This is done by controlling the vertical position of the sample (or the cantilever) via a piezo, which is called as Z-piezo. The control signal for driving the Z-piezo is interpreted to obtain the topography of the sample. The sample is scanned line-by-line, and acquired topographies for each line are used to compose the overall image of the sample via AFM software. Even though the type of motion of the cantilever during the scan, type of sensors and detection techniques vary in different types of AFM, they all operate according to this principle. General structure of the AFM is given in Figure 2.1, which uses the Optical Beam Deflection (OBD) technique (Viani et al., 1999) that is very common in most of the AFM systems for detecting the amount of cantilever deflection.

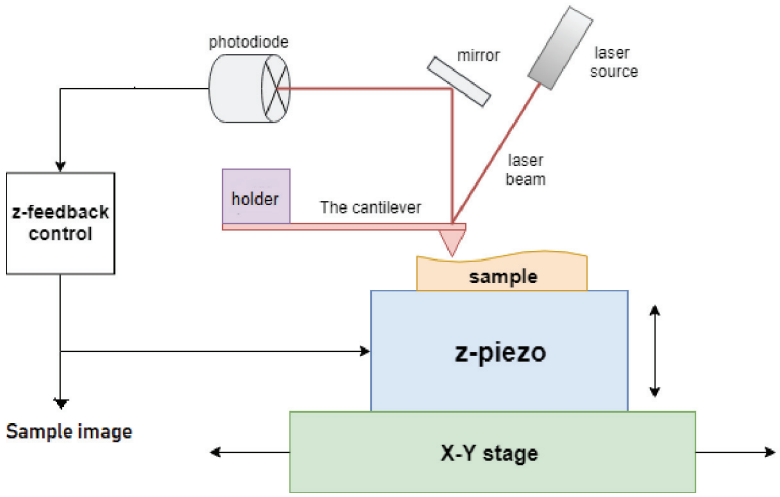

Figure 2.1. General structure of the AFM

There are several ways of sensing the deflection rate of the cantilever, such as using a piezoresistor at the cantilever's fixed end, using capacitive detection between a conductive sample and a conductive cantilever, using piezoelectric cantilevers, or the OBD method. A piezoresistor at the fixed-end changes its resistance when the cantilever yields to a stress on it while bending upwards and downwards, thus the amount of deflection can be detected due to the change in the voltage drop on the piezoresistor. Capacitive detec-

tion is an option for conductive samples and cantilevers, based on detecting the change in capacitance between the cantilever and the sample since the capacitance between them changes due to the change in distance between their surfaces. Piezoelectric cantilevers generate a voltage when they bend due to tip-sample interaction forces, thus the deflection rate can be detected by measuring the voltage it outputs. In the well-known OBD technique, a laser beam is focused onto the point on the cantilever, which is close to the location of the tip, and it is reflected by the cantilever's surface. Reflected beam is focused onto a photodiode via a mirror. After the scan starts, attractive and repulsive tip-sample interaction forces arise between the tip and the surface atoms, whose type and intensity depends on the distance between them as explained in the next Chapter. These forces make the cantilever deflect towards the direction of the interaction force. Therefore, the laser beam is reflected by the cantilever's surface with a different angle than before. Since the output voltage depends on the point where the reflected laser beam drops on the photodiode, the amount of deflection can be detected by comparing initial and current photodiode output voltages.

Photodiode output is used as the control variable in Z-feedback, as in Figure 2.1. Thus, set-point for the control is the desired photodiode output. As mentioned before, Z-feedback control serves for controlling the vertical position of the sample (or in some AFMs, the cantilever) during the scan through Z-piezo. According to the type of AFM, it may serve to keep the cantilever oscillation amplitude or frequency constant. It is critical for accurate imaging of a sample without damaging it. If the scanned material is very soft, the tip may be buried into the sample or the sample may be swept away with the tip. On the other hand, the scanned sample may be stiff, and the tip may scratch or drill its surface. Bandwidth of the controller should be as high as possible in order to actuate the Z-piezo without a critical delay in response to a change in topography while the tip traces the surface.

2.2. Operating Modes

AFM can be divided into two types in general in terms of cantilever motion during the scan; Static-AFM (contact-mode) and Dynamic-AFM. Dynamic-AFM can also be grouped into two types in the same way; tapping-mode and non-contact mode. These are illustrated in Figure 2.2. Along with the different cantilever excitation methods, two types of detection technique is used in Dynamic-AFMs; Amplitude Modulation (AM-AFM) and Frequency Modulation (FM-AFM). Here, working principles of these types of

AFM are explained.

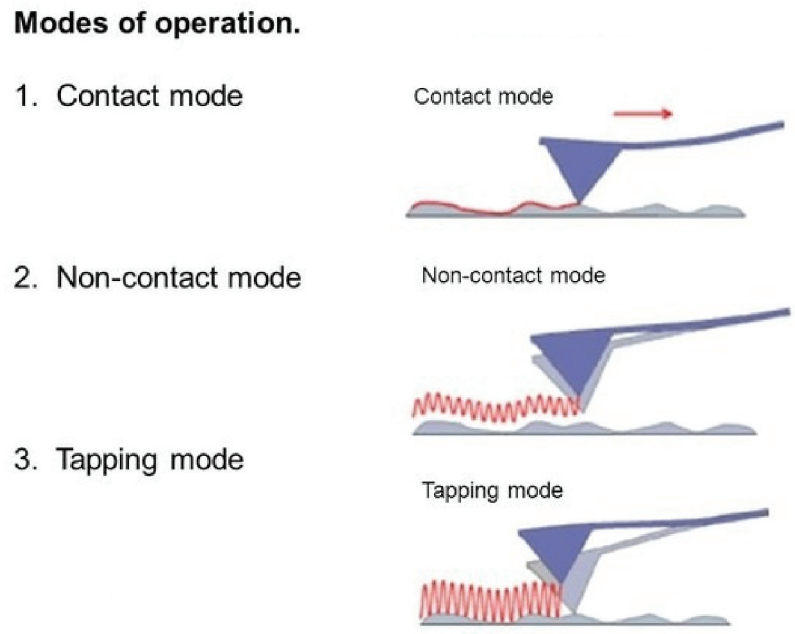

Figure 2.2. Modes of the AFM in terms of the cantilever motion during the scan. (Source: (quora.com, 2018))

In the Static-AFM, the cantilever beam is kept at rest, and the sharp tip touches the sample surface while tracing the surface. During the scan, it traces exactly the topography, and deflects when there is a feature (peak or hollow) due to tip-sample interaction forces. It goes upwards with a peak and downwards with a hollow on the surface. Thus, the photodiode output changes in phase with the topography. However, vertical position of the sample is still controlled via Z-feedback to prevent strong tip-sample interaction forces, and to protect the sample. In this type of AFM, since the cantilever is static and only deflects due to a change in topography, set-point voltage and the photodiode output voltage are rather slowly changing signals, which are easy to compare. Thus, this is the least complex type of AFM. On the other hand, even though the Z-feedback control is in action, there is still a risk of damaging the material if the bandwidth (or response speed) of the control is not enough to compensate a dramatic change in surface topography during the scan. Additionally, since the tip touches the surface, lateral forces arise on the sample, such as frictional force. This limits the scan speed and may corrode the tip in the long term. Since soft materials are tend to stick to the tip, contact mode is not preferred for biological materials or other types of soft samples.

In the Dynamic-AFM, cantilever is vibrated with a constant frequency, and it os-

cillates over the sample surface with a constant amplitude. In this type of AFM, two types of operation can be preferred; tapping-mode and non-contact mode. The contact time between the tip and the sample is very short in tapping-mode compared to the Static-AFM, and there is no contact in non-contact mode. Thus, smaller tip-sample interaction forces arise in this type of AFM compared to the Static-AFM, which is suitable for soft samples. Additionally, the tip motion and the topography is not identical, and photodiode output does not give an idea about the topography exactly. Since the cantilever is continuously oscillating, the photodiode outputs a high-frequency sinusoidal voltage rather than a slowly changing voltage. Here, oscillation amplitude and frequency of the cantilever change due to the effect of attractive & repulsive tip-sample interaction forces, and the topography change is detected from these data (Garcia and Perez, 2002).

In AM-AFM, the cantilever is vibrated at a constant frequency near (or equal) to its natural resonance frequency f_0. This excitation is done with an electrostatic piezo (dither piezo) attached to the base (fixed-end) of the cantilever. When a sinusoidal voltage is applied to the electrostatic piezo, it periodically expands and squeezes. This motion of the piezo in turn vibrates the cantilever through its holder. According to the quality of the dither piezo, cantilever vibrates with a constant amplitude and frequency. When there is no external force acting on the cantilever beam, amplitude of its oscillation is in the maximum level, which is called as the free-air amplitude A_0. Amplitude of the cantilever oscillation is detected at the output of the photodiode via electronic circuits, such as rms-to-dc converter (envelope detector) or peak detector. Control variable and set-point of the Z-feedback are the measured amplitude and desired amplitude of the output voltage, respectively. General structure of an AM-AFM is given in Figure 2.3.

Output of the amplitude detector is subtracted from the set-point amplitude, which is the amplitude of a reference voltage that the photodiode outputs when the cantilever oscillation amplitude is at the desired level. In this way, the error signal for Z-feedback controller is generated. Before the scan starts, the controller adjusts the tip-sample distance through Z-piezo so that the oscillation amplitude becomes equal to the set-point amplitude. Then, the tip starts to trace the surface by tapping it in each cycle. The controller acts when the tip faces a feature (dip or hill) on surface since the oscillation amplitude changes. The control signal provided by the controller gives the surface topography. Control signal is amplified and interpreted by computer software for obtaining the image of the surface.

In some AM-AFM applications, the cantilever is vibrated with a very small amplitude (e.g. less than 1 nm), and it stays in the attractive region. The cantilever is in the

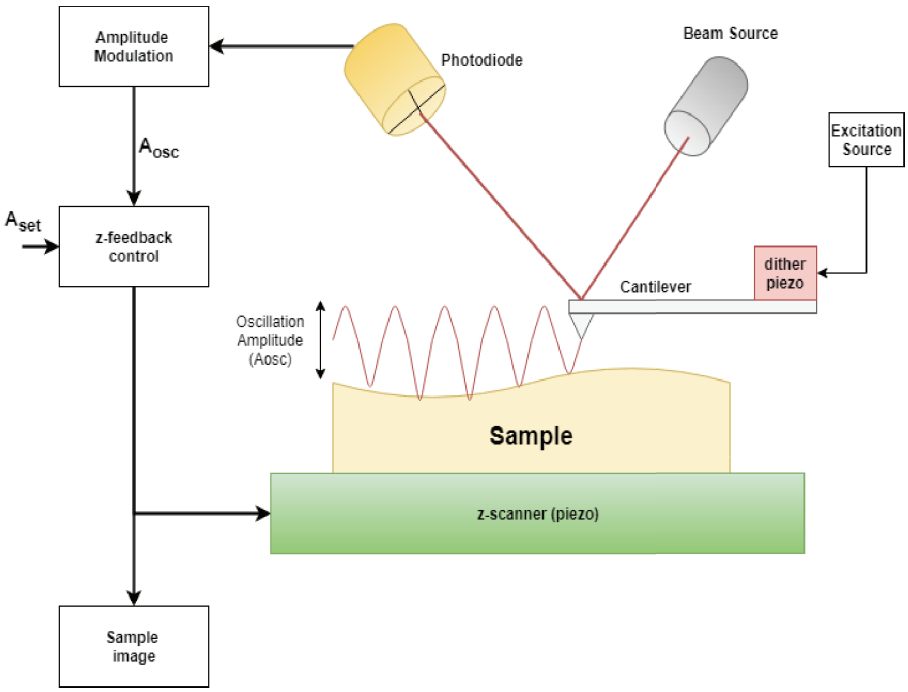

Figure 2.3. Structure of the AM-AFM

attractive region where the distance between the cantilever tip and the sample is more than interatomic distance (0.2 nm). This means that cantilever does not "touch" the surface during the scan. On the other hand, in majority of the AM-AFM systems, the cantilever is permitted to touch the surface while oscillating. The tip comes into contact with the sample for a very short time, basically "taps" the surface, at each cycle of the oscillation. This type of AFM is called as tapping-mode AFM.

In FM-AFM, cantilever is vibrated at a frequency f, different from the cantilever's natural resonant frequency f_0, with a constant amplitude or excitation. In contrast to AM-AFM, the cantilever is not excited via an external excitation source. Instead of this, the excitation signal comes directly from a positive feedback loop, like a self-driven oscillator. In addition to this, the scan is performed in non-contact mode. The measurement signal that is generated by the photodiode is amplified and phase shifted, and used to vibrate the cantilever. For detection of the topography change, a different physical phenomena that occurs due to tip-sample interaction is used. When the cantilever comes closer to the sample, since the cantilever is now self-oscillating, its oscillation frequency changes due to tip-sample interaction forces. Amount of the frequency shift depends on the intensity of the tip-sample interaction force, and this frequency shift is used to detect a change in topography during the scan. Another feedback loop, which is the Z-feedback control, serves for controlling the vertical position of the sample to keep the frequency shift Δf

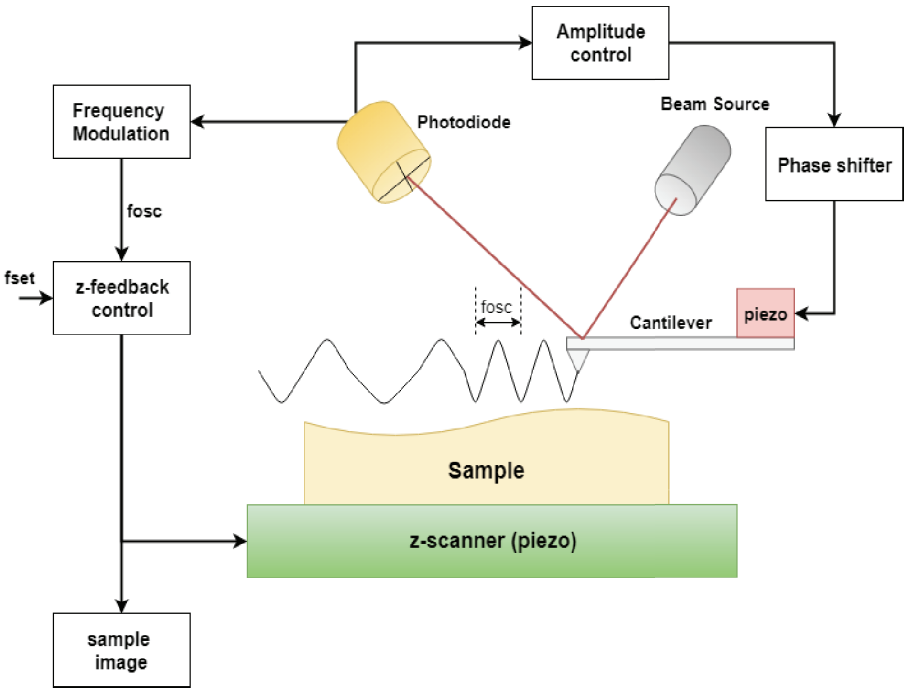

Figure 2.4. Structure of the FM-AFM

constant. Structure of the FM-AFM is given in Figure 2.4. Since a higher quality factor is desired to increase sensitivity, FM-AFM is more suitable for applications in ultra high-vacuum (UHV) environment.

2.3. High-Speed AFM Studies

After the invention of AFM and the development of its types explained above, one of the main motivations behind the improvements of the AFM has become increasing the scan speed. Scan rate of an AFM is generally expressed in terms of the frame rate, which is the number of frames that the AFM can capture in a second, i.e., frames per second (fps). A high frame rate is necessary to capture specific processes which occur very fast, such as biomolecular dynamic processes, corrosion in material science, or self-assembly processes (Liu et al., 2017). Furthermore, a high scan rate shortens the tip-sample interaction time and thus, minimizes the intensity of tip-sample interaction forces. However, the scan rate is chosen according to the capability of both the Z-actuation and X-Y scanners in AFM. There are also other factors that limit the scan speed such as resonance frequency of the cantilever and the speed of electronic detector.

In the early period that AFM has become widely used in research studies, scien-

Figure 2.5. A real-time HS-AFM system (Source: (benmoshe.net, 2017))

tists that especially working on investigating biological processes pointed out the need of high-speed AFM systems because of the facts expressed above. Since the beginning of 1990s, numerous research groups including the ones leaded by Hansma (Hansma et al., 2006), Schafer (Schafer and Braunsmann, 2010), Miles (Humphris et al., 2005), and Ando (Ando, 2012) have worked on the improvements of AFM to obtain high-speed AFM, in order to observe some bio-dynamical processes, such as living cells (Schitter et al., 2004), proteins and DNA/RNA (Barzanilla et al., 1994; Guthold et al., 1994; Kasas et al., 1997; Guthold et al., 1999). Several studies have been conducted to try new control methods (Wang et al., 2015, 2016; Peng et al., 2015; Chuang et al., 2013; Schitter et al., 2001; Nakakuki et al., 2012), and to develop new sensors, actuators and cantilevers via the MEMS technology (Ando, 2012; Lee et al., 2006), or new scan methods (Zhang et al., 2018) in order to enable higher scan rates in AFM. To eliminate the risk caused by high quality factor in air and high-vacuum, Q-control method that minimizes the quality factor of the cantilever has been developed (Ando, 2014; Balantekin, 2015). Ando and his group succeeded to come up with an high-speed AFM system that is capable of capturing bio-dynamical processes clearly in 2008 (Ando, 2012). An example of a real-time HS-AFM system having the Ando's structure is shown in Figure 2.5. With the state-of-the-art HS-AFM they developed, they could capture the video images of protein molecules, molecular machines made by proteins (Ando, 2013) and walking myosin V (Kodera et al., 2010). An example of a biodynamical process captured by the HS-AFM, which is the image of

the dynamical behavior of the lithosthatine protofibril is shown in Figure 2.6.

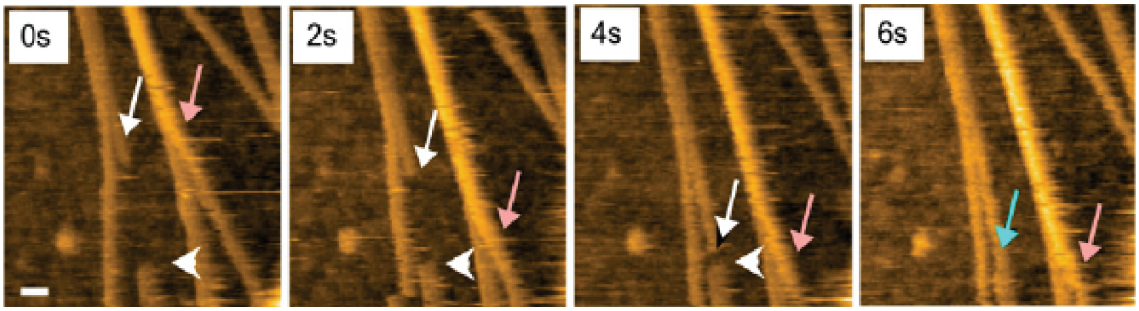

Figure 2.6. HS-AFM images showing the time lapse of lithosthatine protofibril elongation and association (Source: (Ando, 2012))

The high-speed AFM system that Ando's group has developed has a structure of tapping-mode amplitude modulation AFM (AM-AFM). In their system, a small high-frequency cantilever that was designed in cooperation with Olympus Inc. is used as the scanning probe. It has 1.2 MHz resonance frequency and spring constant of 0.2 N/m in liquid, 3.5 MHz resonance frequency and spring constant of 0.3 N/m in air. This type of cantilever enables a fast scan due to its high resonance frequency, and since its spring constant is quite low, it is soft enough to not to harm the soft biological specimen. Thus, the HS-AFM system they developed is intended to be a tool for observing especially bio-dynamical processes. Figure 2.7 shows the SEM (Scanning electron microscope) images of a conventional AFM cantilever and a small high-frequency cantilever as an illustrative for the difference between dimensions of them.

They also used the angle-based optical beam deflection (OBD) for cantilever deflection measurement, which is more advantageous and accurate than other distance-based detectors available in commercial AFM systems. Furthermore, the high-speed scanner they developed by using an active damping technique, which is based on Q-control, and a mock Z-scanner made a remarkable impact to increase the actuation speed. The bandwidth of the Z-piezo in this actuator is 370 kHz, and they claim that the frame rate that can be achieved under certain conditions with this Z-scanner is up to 25 fps.

Although they could improve the scan rate by using a high-frequency cantilever, a faster piezo and detection system, Z-feedback bandwidth that they can achieve is maximum of 100 kHz (Ando, 2012). Also, the error signal saturation phenomena that occurs at falling edges of features on the topography (Sulchek et al., 2002), which is explained in Chapter 4, limits the maximum scan rate. Ando solved this problem via dynamic PID control method, which is based on augmenting the very low error signal at the falling

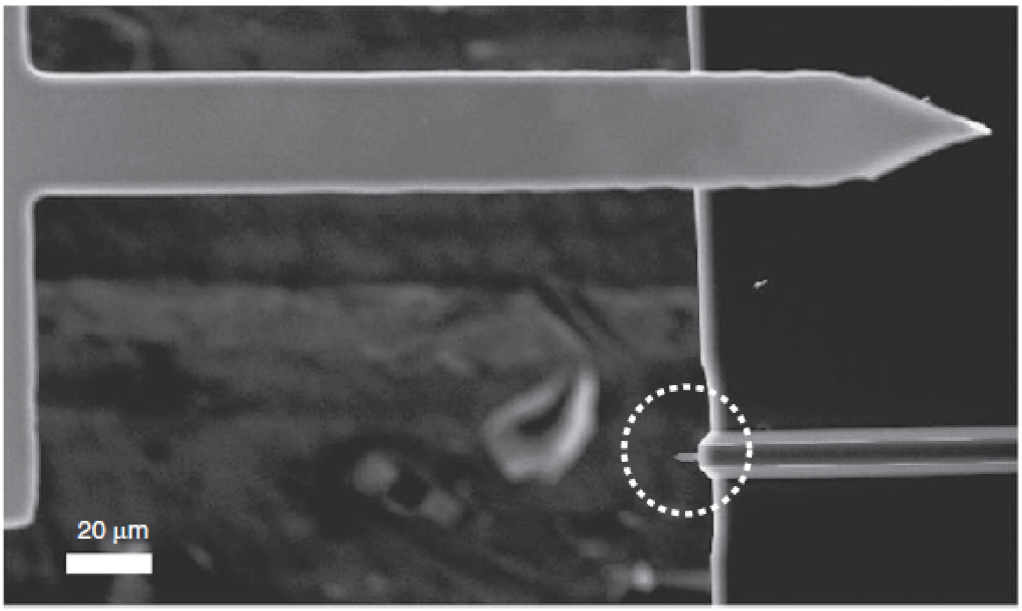

Figure 2.7. SEM image of a conventional AFM cantilever (Olympus OMCL-AC240TS) and a small high-frequency cantilever for HS-AFM (Olympus BL-AC10DS; encircled) (Source: (Uchihashi et al., 2012))

edge of the sample topography via an additional gain before the controller, to improve the controller response. Thus, they enhanced the capability of topography acquisition of the system in high scan rates.

CHAPTER 3

SYSTEM MODEL

As mentioned in the previous chapter, the state-of-the-art HS-AFM that Ando's group has developed (Ando, 2012) is modeled in SIMULINK for the controller design in this study. The modeled system is a tapping-mode AFM. The cantilever with its first three flexural eigenmodes, the tip-sample interaction force, and the Z-piezo that actuates the sample in z-axis during the scan are implemented with their equivalent models, in SIMULINK. The amplitude detector to measure the peak-to-peak value of the cantilever oscillation, and the false error method used to minimize the error signal saturation are implemented with their dynamic models. PI and H_∞ controllers are implemented via their continuous-time transfer functions. For each cantilever, simulations are performed for both PI and H_∞ controllers under the same conditions and at the same time interval. Naturally, the parameters of the controllers in the model varies for each cantilever.

Some elements in the system are taken as ideal, i.e., their transfer functions are unity, such as the dither piezo that is used to vibrate the cantilever, and the quadrant photodiode that converts the reflected laser beam into voltage according to the cantilever deflection rate. This is preferred, since the study focuses on the effect of controller, and taking these elements as ideal does not change the result. Thus, only the key elements in the Z-feedback are modeled with their actual dynamics. General structure of the system used in this study is given in Figure 3.1. Methods for implementing each element in the system model are explained in the following sections.

3.1. Cantilever Model

Cantilever is a micro-machined beam that has a mass, stiffness and damping due to its material properties, and it bends when a force applied on it. When a constant force is applied at a point on it, except its fixed-end, it bends in the direction of the force. When a sinusoidal force is applied, it starts a harmonic motion. When the frequency of the force source is close or equal to its resonance frequency, the cantilever starts to oscillate with a constant frequency and amplitude. Total motion of the cantilever is expressed in terms of modal shape functions, the point where the force is applied and its material properties

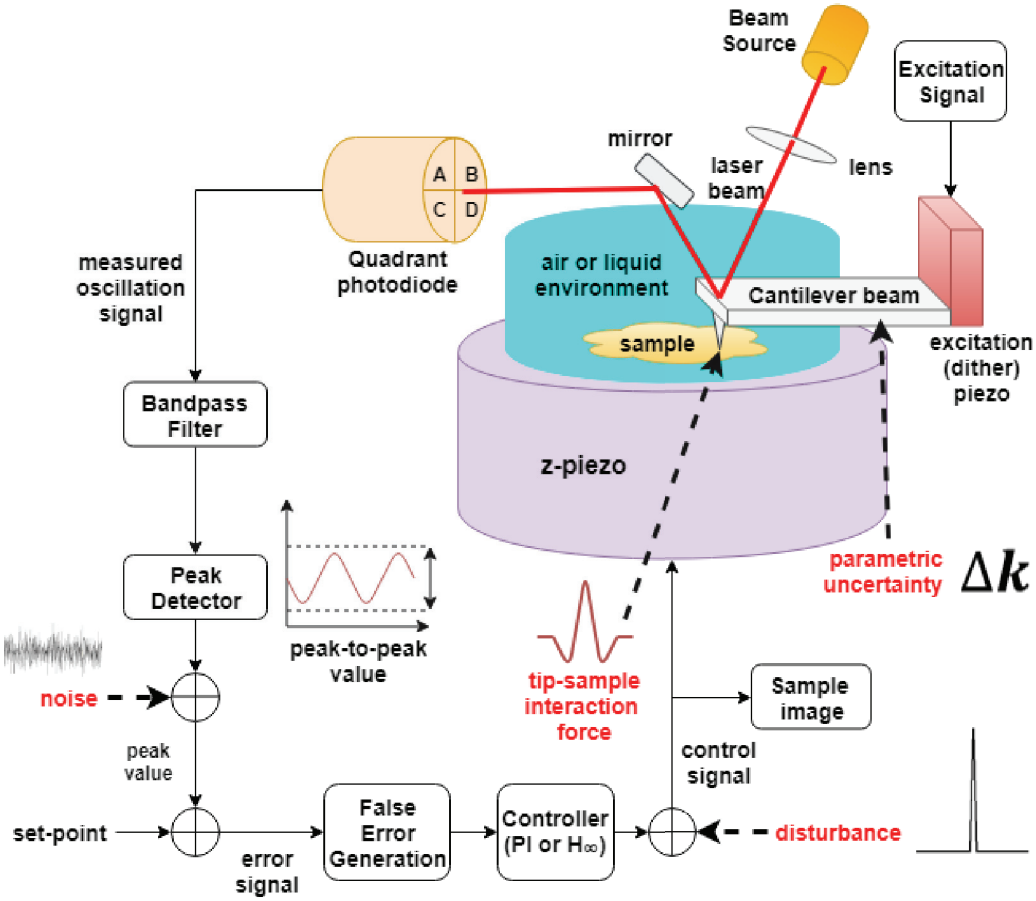

Figure 3.1. General structure of the state-of-the-art HS-AFM system used in this study

(mass, damping, stiffness) in response to the intensity of the applied force (Ryba, 2006). On the other hand, in order to find the current position of a single point on the free end of the cantilever, this expression can be simplified into a mass-spring-damper model. As in the state-of-the-art HS-AFM system used in the study, excitation force is applied from the fixed-end of the cantilever via the dither piezo.

Assuming the initial position of the tip as 0, its current position x can be expressed via mass-spring-damper equation as

$$m\ddot{x} + b\dot{x} + kx = F_{drive} + F_{int} \tag{3.1}$$

where m is the mass, b is the damping constant and k is the spring constant of the cantilever. F_{drive} is the excitation force that vibrates the cantilever, and F_{int} is the tip-sample interaction force. Equation (3.1) is manipulated by using the relations given in 3.2 and 3.3.

$$\omega_0 = \sqrt{\frac{k}{m}} \tag{3.2}$$

$$\frac{\omega_0}{Q} = \frac{b}{m} \tag{3.3}$$

where ω_0 is the resonance frequency of the cantilever in radians per second and Q is the quality factor of the cantilever, respectively. Hence, Equation (3.1) can be converted to

$$\ddot{x} + \frac{\omega_0}{Q}\dot{x} + {\omega_0}^2 x = \frac{{\omega_0}^2}{k}(F_{drive} + F_{int}) \tag{3.4}$$

As mentioned before, the cantilever model is established by using its first three flexural eigenmodes. An elastic structure like a cantilever beam shows a peculiar response at a particular frequency, and this response does not occur at a single frequency, but at several frequencies. These frequencies are called the eigenmode resonance frequencies. These eigenmodes could be flexural, torsional, or lateral eigenmodes. In tapping-mode, the normal tip-sample interaction forces are in effect and only the flexural eigenmodes are taken into account to obtain the tip displacement. In each flexural eigenmode, the spring constant k and the quality factor Q of the cantilever also varies. The point-mass model for each flexural eigenmode can be expressed as

$$\frac{k_i}{{\omega_i}^2}\ddot{x}_i + \frac{k_i}{\omega_i Q_i}\dot{x}_i + k_i x_i = F_{drive} + F_{int}(d) \tag{3.5}$$

w_i, k_i and Q_i are the resonance frequency, spring constant, and quality factor of the i'th flexural eigenmode, respectively. The tip-sample distance, d, can be found from the tip position x and the sample position x_s as $d = x - x_s$. Actual position of the tip x is found from the contributions of three eigenmodes as $x = x_1 + x_2 + x_3$.

This procedure is followed for four cantilevers employed in the state-of-the-art HS-AFM system in this study. For the low-frequency (large) cantilever in air, Olympus AC-160TS is used. For the high-frequency (small) cantilever in the same environment, NanoWorld USC-F5-k30 is preferred, due to the fact that in air environment, soft cantilever can easily stick to the sample surface. Meanwhile, for the liquid environment, NanoWorld USC-F0.3-k0.3 is used as the low-frequency cantilever, and the cantilever used in Ando's HS-AFM (Ando, 2012), which is manufactured by Olympus, is preferred

as the high-frequency cantilever. k and ω_0 of the 1st eigenmode of each cantilever are obtained from the manufacturer, and rectangular beam formula is used to calculate these parameters for higher eigenmodes (Kokavecz and Mechler, 2008). Q of the 1st eigenmode of the cantilevers are taken as 150 in air and 2 in liquid, since these are the values typically measured in a tapping-mode AFM experiment. In order to find the quality factor of the 2nd flexural eigenmmode Q_2, Q-factor of the 1st eigenmode is doubled. Same procedure is followed to find Q_3 from Q_2. This is preferred as measured Q-factors of the flexural eigenmodes are commonly have this ratio in real-time. Properties of these cantilevers for the first three flexural eigenmodes, which are found via rectangular beam formula, are given in Table 3.1.

Table 3.1. Properties of the four cantilevers used in this study including their three flexural eigenmodes used in the study

Eigenmode (n)	**Spring Constant (k_n) (N/m)**	**Quality factor (Q_n)**	**Resonance Frequency (f_n) (MHz)**
Low frequency cantilever in air (Olympus AC-160TS)			
1	26	150	0.3
2	1031	300	1.9
3	7962	600	5.3
High frequency cantilever in air (NanoWorld USC-F5-k30)			
1	30	150	5
2	1190	300	31.5
3	9187	600	87.5
Low frequency cantilever in liquid (NanoWorld USC-F0.3-k0.3)			
1	0.3	2	0.3
2	12	4	1.9
3	92	8	5.3
High frequency cantilever in liquid (Ando, 2012)			
1	0.2	2	1.2
2	8	4	7.6
3	61	8	21

Dynamic systems can be implemented as state-space in SIMULINK environment. State-space of the every eigenmode i is obtained by using the models (3.4) and (3.5) as

$$\begin{aligned} \dot{x_i} &= z_{1i} \\ x_i &= z_{2i} \\ \begin{bmatrix} \dot{z}_{1i} \\ \dot{z}_{2i} \end{bmatrix} &= \begin{bmatrix} -\frac{\omega_i}{Q_i} & {\omega_i}^2 \\ 1 & 0 \end{bmatrix} \begin{bmatrix} z_{1i} \\ z_{2i} \end{bmatrix} + \begin{bmatrix} \frac{{\omega_i}^2}{k_i} \\ 0 \end{bmatrix} (F_{drive} + F_{int}) \end{aligned} \tag{3.6}$$

The amplitude of the excitation source is chosen such that it yields a free-air peak oscillation amplitude of 5 nm. In order to do so, the driving force F_D is chosen according to the formula

$$A_0 = \frac{F_D Q_1}{k_1} \tag{3.7}$$

in which F_D is the amplitude of the excitation force, Q_1 and k_1 are quality factor and spring constant of the 1st eigenmode. Drive force frequency is chosen to be the resonance frequency of the 1st eigenmode of the cantilever (ω_1). It is implemented as a sine wave in SIMULINK. By adding a DC offset to the sinusoidal excitation source of the cantilever, the initial distance between the tip and the sample is adjusted.

3.2. Tip-Sample Interaction Forces

The major exogenous effect on the cantilever motion during the scan in AFM is the interaction force that arise between the tip and the sample surface. This phenomena is caused by electromagnetic fluctuations and ionic repulsion between the tip and sample atoms (Garcia and Perez, 2002). The intensity and the type of these forces vary due to tip-sample distance. If the tip-sample distance is higher than the inter-atomic distance a_0, 2 Angstroms (0.2 nm), attractive van der Waals forces are in action. Under the effect of this force, the tip and the sample atoms basically attract each other and the tip tends to approach the sample. This bends the cantilever towards the direction of the sample. Since the cantilever is located above the sample, the direction of the van der Waals force is accepted as in -z direction. When the tip and the sample are very far away, the van der Waals forces are very weak and the cantilever's oscillation amplitude is maximum, i.e., equal to the free-air amplitude A_0. When the tip comes closer to the surface, the van der Waals forces increase and reach to the maximum level when the tip-sample distance is equal to the inter-atomic distance a_0, as shown in Figure 3.2. If the tip-sample distance

is lower than or equal to a_0, the tip and the sample atoms starts to repel each other and the repulsive force emerges. In this study, these forces are modeled via Derjaguin-Müller-Toporov (DMT) model. According to the DMT model, the interaction force is expressed as

$$F_{int}(d) = \begin{cases} -\dfrac{HR}{6d^2}, & d > a_0 \\ -\dfrac{HR}{6{a_0}^2} + \dfrac{4}{3}E^*\sqrt{R}(a_0 - d)^{3/2}, & d \leq a_0 \end{cases} \tag{3.8}$$

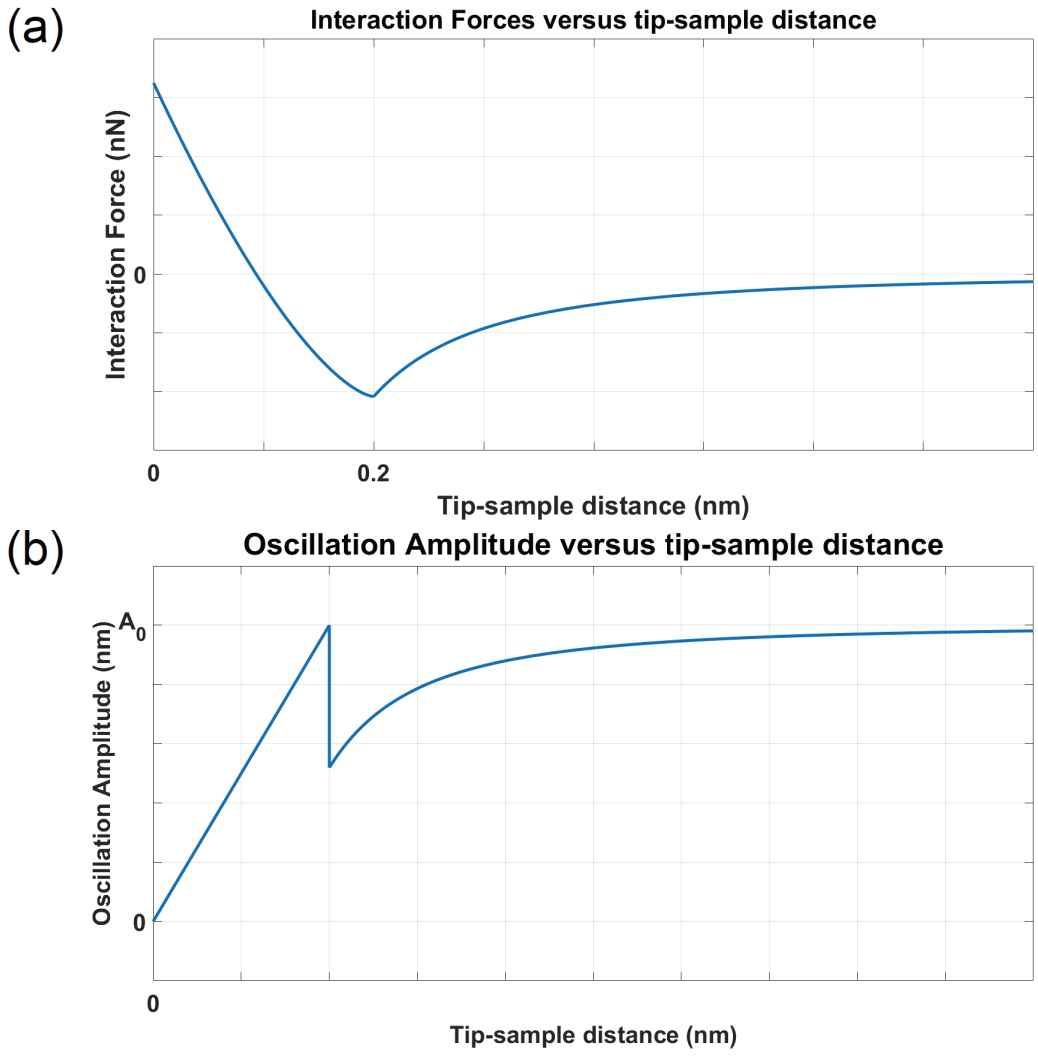

Figure 3.2. The graphs illustrating the relationship of a) Amplitude of tip-sample interaction forces b) Cantilever oscillation amplitude versus tip-sample distance

where d is the tip-sample distance, H is the Hamaker constant, R is the tip radius and E^* is the effective tip-sample elasticity. Each cantilever used in this study have the

same tip radius of 5 nm and effective tip-sample elasticity of 20 GPa. Hamaker constant is 10^{-19} in air and 10^{-20} in liquid. In the second case, the total interaction force is the sum of the van der Waals and repulsive forces. The repulsive force becomes more dominant after the tip-sample distance drops to a certain level and resulting interaction force becomes positive. In the system model, F_{int} is generated via MATLAB function that computes the tip-sample distance d as expressed in Section 3.1, and the conditional statement in (3.8). This force is added to the drive force, as in (3.5).

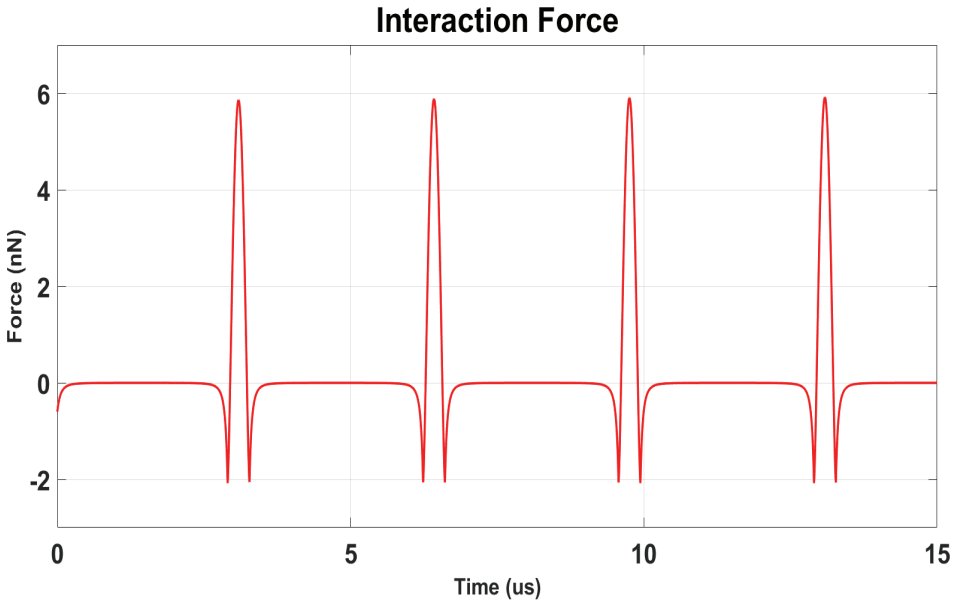

Figure 3.3. Waveform of the interaction forces in steady-state in tapping-mode AFM

Van der Waals forces decrease the oscillation amplitude until the tip-sample distance drops to a certain level. At certain distance, the oscillation amplitude changes abruptly due to the bistable phenomena in tapping-mode AFM (Balantekin and Atalar, 2003). Beyond this point, the decreasing oscillation amplitude is attributed to the strong repulsive forces. Relationship between the tip-sample distance, interaction forces and oscillation amplitude in Dynamic-AFM is shown in Figure 3.2.

When cantilever oscillations reach their steady-state, the tip comes to a distance from the sample surface such that the oscillation amplitude becomes equal to the set-point amplitude in Z-feedback control. In conclusion, interaction forces follow the waveform as shown in Figure 3.3.

3.3. Z-Piezo

In AFM, controller drives the Z-piezo, in response to the topography changes that the tip faces while tracing the sample surface. It can be either attached to the cantilever base, or it can be attached to the holder of the sample. In the first case, sample position is constant and does not change, while the cantilever holder is moved down or up. In the latter case, the Z-scanner is used to change the sample position. Thus, the Z-piezo is the actuator of the Z-feedback control. As the state-of-the-art HS-AFM system model used in this study is inspired from Ando's HS-AFM system (Ando, 2012), second case is applied to the system model of this study.

Dynamics of a piezo can be expressed via mass-spring-damper model like the cantilever model generated in this study. Only difference is that the input of the dynamic system is the applied voltage instead of the applied force. Input voltage that drives the Z-piezo is provided by the controller, and it is used to obtain the sample image at the same time. In this study, Z-piezo is also modeled via ODE of a mass-spring-damper model as in (3.9), and its parameters are taken from the parameters of the Z-scanner used in Ando's HS-AFM.

$$\ddot{x}_s + \frac{\omega_p}{Q_p}\dot{x}_s + {\omega_p}^2 x_s = \frac{{\omega_p}^2}{k_p} V_{in} \tag{3.9}$$

where ω_p, Q_p and k_p are the resonance frequency, quality factor and spring constant of the piezo, respectively. x_s is the current position of the sample, which is subtracted from the tip position x to obtain the tip-sample distance d. Equation (3.9) is implemented as state-space in SIMULINK as in the cantilever model.

Parameters of the Z-scanner of the HS-AFM that is modeled in this study are taken from the literature (Ando, 2012). The bandwidth of Z-scanner is 370 kHz, and its Q-factor is taken as 1.5 as it is given in the range of 1-2. Spring constant k_p is chosen arbitrarily as 1. It is seen that the response of Z-scanner is quite satisfactory, as its bandwidth is high enough to respond fast to a change. Additionally, since Q=$\frac{1}{2\zeta}$, where ζ is the damping ratio, and the Q-factor of the Z-scanner is 1.5, its response is close to the critically damped one (ζ=0.5). This is desired to have the fastest response without overshoot.

3.4. Amplitude Detector

As HS-AFM is a type of AM-AFM, the cantilever and thus, the sharp tip at its free-end oscillates along z-axis, and the photodiode outputs a sinusoidal signal. Since it is a time-varying signal, it cannot be compared with a constant reference. Choosing a sinusoidal reference and comparing with the measured signal in real-time is problematic, as direct subtraction of two time-varying signals may yield an inaccurate result due to phase shifts. Because of this, rms-to-dc converter or amplitude detector circuits are employed at the output of the photodiode in AM-AFM systems (Balantekin and Degertekin, 2011; Ando, 2012). In this way, instead of the output signal itself, its amplitude is found and used as the control variable. Set-point (reference) for the Z-feedback is the desired oscillation amplitude. It is easy to compare the oscillation amplitude with a constant reference, and yields to a more accurate control.

To find the peak-to-peak amplitude of the oscillation, an amplitude detector is developed for the state-of-the-art HS-AFM system used this study, as it is faster compared to the rms-to-dc converter. Its working principle is very similar to the peak detector circuit that is used in (Balantekin and Degertekin, 2011). Only difference is that instead of capacitors and switches, gates that are triggered via pulse generators and min/max functions that find the minimum and maximum value of the input signal are used in SIMULINK environment. Period of the pulse generators are adjusted such that in the first half cycle, maximum value of the input is found and registered to the output at the end of the half-cycle. Minimum value of the second half-cycle is found via the same procedure. Peak-to-peak amplitude is found by subtracting the minimum value from the maximum value at the output. Output of the amplitude detector with respect to the cantilever oscillations, and lower & upper envelopes of the oscillation which is detected by min/max functions of the peak detector, are given in Figure 3.4.

As explained in the first section of this chapter, the cantilever is modeled with its first three flexural eigenmodes to have a more realistic result. Each eigenmode contributes to the total motion of the cantilever but the first eigenmode is dominant by far. However, contribution of these eigenmodes may cause problems in Z-feedback control unless special care is taken in amplitude detection. There are cases that very small changes in controller gains cause ringings or even instability because of the contribution of higher eigenmodes. To prevent this problem, contributions of 2nd and 3rd flexiral eigenmodes in the cantilever oscillation are eliminated via a bandpass filter that is used before the amplitude detector. Thus, only the 1st eigenmode is used for the amplitude detection. A

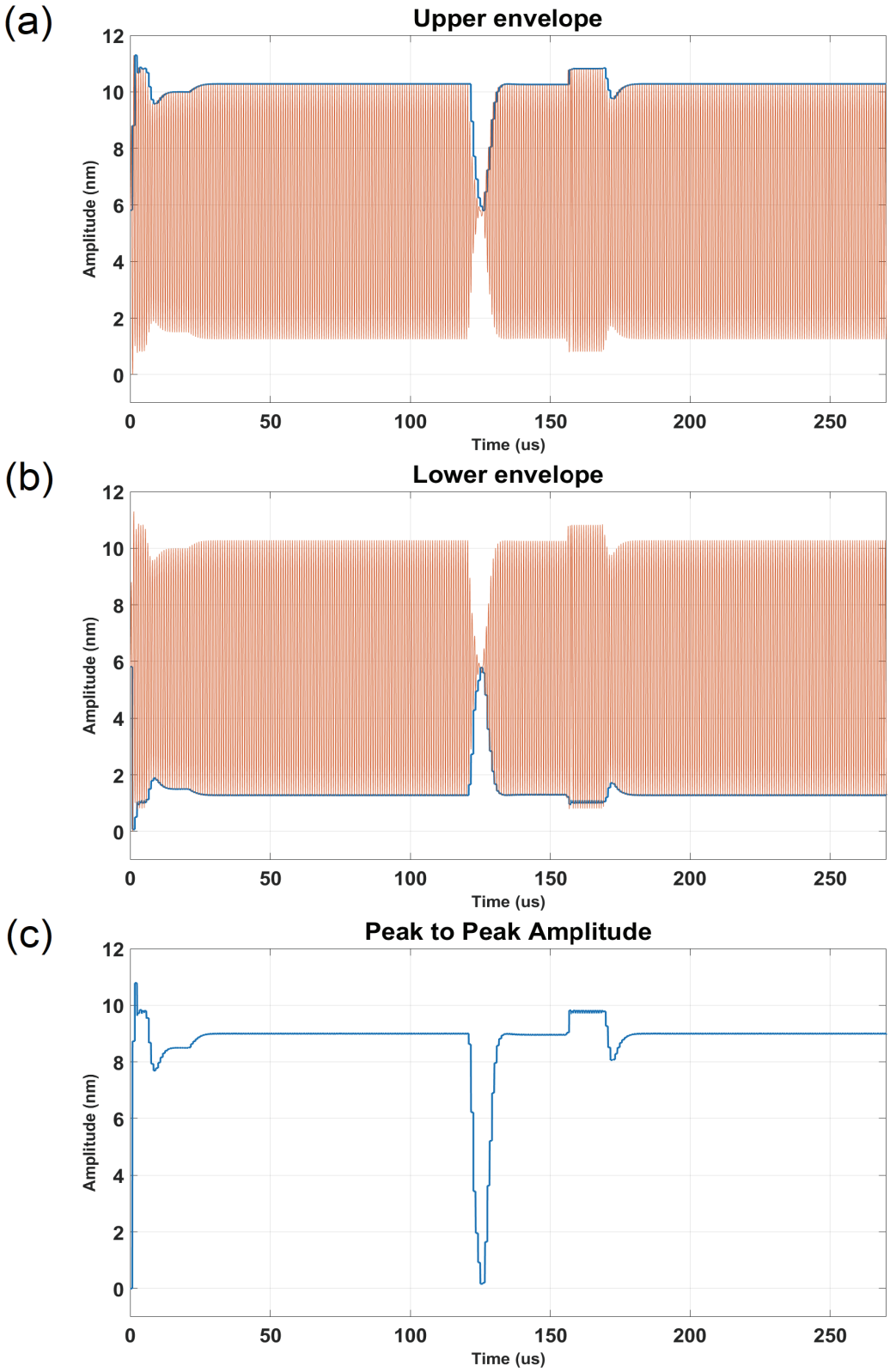

Figure 3.4. a) Upper envelope of the cantilever oscillation b) Lower envelope of the cantilever oscillation c) Peak-to-peak amplitude at the output of the amplitude detector

second order bandpass filter is preferred for each cantilever used in the state-of-the-art HS-AFM model, whose center frequency and passband are chosen as equal to the resonance frequency of the 1st eigenmode. Since the closest resonance frequency, which is the 2nd eigenmode, is equal to approximately 6.3 times the resonance frequency of the 1st eigenmode (Kokavecz and Mechler, 2008), 2nd and 3rd eigenmodes are successfully eliminated in this way.

CHAPTER 4

CONTROLLER DESIGN

In this study, PI controller, usually used in commercial AFM systems and the state-of-the-art high-speed dynamic AFM system, and H_∞ controller, a nonlinear controller prominently proposed in the past years for HS-AFM in the literature, are designed for the modeled state-of-the-art HS-AFM system. Since the system dynamics change with each cantilever used, four different PI and H_∞ controllers are designed for these cantilevers employed in the modeled system. Set-point peak-to-peak amplitude of the Z-feedback control is chosen as %90 of the free-air peak-to-peak amplitude, i.e., A_{set} = 9 nm.

The controllers are optimized to their most aggressive states. In this state, the closed-loop system can give the fastest response without overshoot. This is done by adjusting the parameters of controllers via analytical methods, which are explained in Section 4.1. and Section 4.2. In this study, since A_{set} = 9 nm (peak-to-peak), most aggressive state corresponds to the case that the cantilever oscillation amplitude becomes 9 nm as fast as possible after the topography change with the used controller. Once optimizing the controllers to the most aggressive state, another method is employed to help the controllers to overcome the error signal saturation phenomenon observed in the falling edges of the sample topography. This method is the false error generation method, which is same as the dynamic PID used in HS-AFM (Ando, 2012; Balantekin and Degertekin, 2011). This method and how it is applied in this study are explained in Section 4.3. The controller parameters adjusted for each cantilever, together with gains used in the false error generation method for each cantilever, are given in Table 4.2.

4.1. PI Controller Design

PID controller and its derivatives (P, PI, PD) are the most common methods used for controller design purposes in the literature. It is easy to optimize and implement for almost any kind of system. Like in many physical systems, a PI controller is employed in commercial AFM and in the state-of-the-art HS-AFM in Z-feedback (Ando, 2012). Gains of the PI controller and the set-point for the Z-feedback control are entered by the user via AFM software in real-time applications (Ramsdell and Gaskell, 2013). So,

these gains and scan rate should be well-defined by the user for a successful result. When the scan is completed, if the chosen PI gains are very low for the defined scan rate, Z-actuation becomes insufficient for a successful topography acquisition, and most of the features on the surface are missed. Hence, the resulting image becomes inaccurate. If the gains are chosen as very high, it yields to oscillations in the controller response and high electronic noise, thus the resulting image again becomes corrupted. If the first obtained result is not satisfactory, PI gains or scan rate should be updated by the user. Scan rate can be decreased for a more accurate detection, but it is not preferred in HS-AFM systems. Therefore, to have high-quality images with high scan rate, choosing the PI controller gains in an appropriate way is crucial.

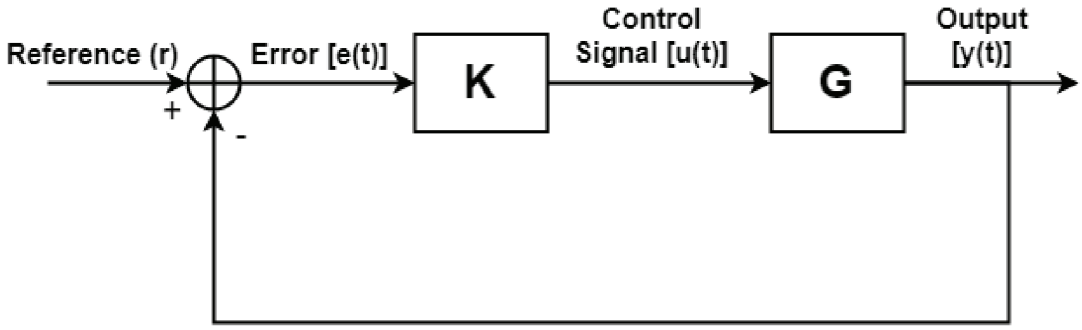

Figure 4.1. General structure of a feedback control loop

PID control is based on minimizing the error between the desired (set-point) and the actual values of the control variable of a feedback system, as shown in Figure 4.1. Here, error $e(t)$ is the difference between the reference r (set-point) and the measured process output $y(t)$. If the error is minimized, output can be equalized to the set-point and the aim of the control is satisfied. This is provided by the controller K, whose function relates the error signal $e(t)$ to the control signal $u(t)$ for the plant G. Plant is the model of the system that is controlled via the feedback. In a feedback control system like in Figure 4.1, it relates the control input $u(t)$ to the process output $y(t)$. With a PI controller K as used in this study, control signal $u(t)$ is expressed in terms of the error signal $e(t)$ as

$$u(t) = K_p e(t) + K_i \int e(t)dt \tag{4.1}$$

where K_p is the proportional gain and K_i is the integral gain. In Laplace domain, it is expressed as

$$U(s) = \underbrace{\frac{K_p s + K_i}{s}}_{K(s)} E(s) \tag{4.2}$$

Since $Y(s) = G(s)U(s)$ and $U(s) = K(s)E(s)$, the closed-loop transfer function which relates the reference R to the output Y is

$$Y = \underbrace{\frac{GK}{1+GK}}_{C(s)} R \tag{4.3}$$

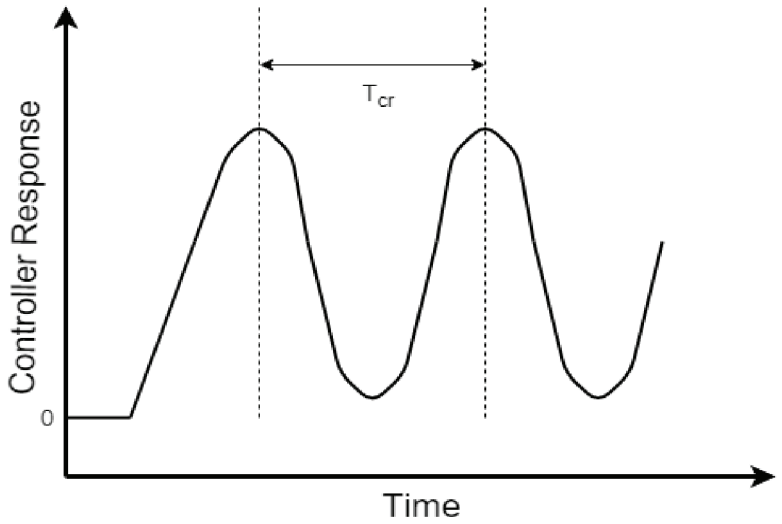

Figure 4.2. Oscillations observed in control signal with critical proportional gain K_{cr}

Here, it is important to find the PI controller transfer function $K(s)$ by choosing the appropriate proportional and integral gains to make the magnitude of the closed-loop transfer function ($|C(s)|$) equal to 1, thus equalizing the reference r to the output $y(t)$. There are various methods available for tuning the PI gains, such as Ziegler-Nichols, Cohen & Coon, AMIGO, Lambda tuning and Internal Model Control (Hyvamaki, 2008). Since the state-of-the-art HS-AFM system used in this study has a nonlinear structure and higher than second order, Ziegler-Nichols ultimate frequency method is chosen for optimizing the PI gains in this study. According to this method, integral gain is made 0 and proportional gain is increased. After a critical proportional gain is achieved, which is denoted as K_{cr}, oscillations with a constant period T_{cr} are observed in the control signal, as shown in Figure 4.2. Critical gain K_{cr} and oscillation period T_{cr} are recorded and used to find the PI gains for each controller by using the formulas given in Table 4.1 (Ziegler and Nichols, 1942). By using the methodology given in Table 4.1, PI gains that are

found for each cantilever in this study are given in Table 4.2. Designed PI controllers are employed in Z-feedback and their performance in topography acquisition in the modeled state-of-the-art HS-AFM is analyzed in the next Chapter.

Table 4.1. Formulas for choosing PID gains from the critical proportional gain K_{cr} and critical oscillation period T_{cr} via Ziegler-Nichols method

Ziegler-Nichols Method			
Control type	K_p	K_i	K_d
P	0.5 K_{cr}	-	-
PI	0.45 K_{cr}	1.2 K_p/T_{cr}	-
PD	0.8 K_{cr}	-	$K_pT_{cr}/8$
PID	0.6 K_{cr}	2 K_p/T_{cr}	$K_pT_{cr}/8$

4.2. Robust H_∞ controller design

Robust H_∞ controller design, which is used as an alternative to the PI controller for comparison in the modeled state-of-the-art HS-AFM, is based on minimizing the H_∞ norm of the closed-loop transfer matrix from exogenous inputs (reference, noise, disturbance) to the errors (reference and tracking errors) by finding an appropriate controller. The controller that satisfies this criterion shapes the frequency responses of the closed-loop sensitivity functions according to the control objectives. Having a good closed-loop response in time domain does not guarantee robustness in response to the exogenous effects in the system, such as noise, disturbances and uncertainties in the system parameters. Thus, frequency characteristics of the controller and the closed-loop sensitivity functions are important to have a good disturbance rejection, noise attenuation and robustness to uncertainties. In physical systems, conditions in the feedback control system are not ideal, as these phenomena are effective on the system dynamics. By knowing this, structure of a feedback control system in Figure 4.1 can be updated with these effects as shown in Figure 4.3.

In the feedback control system as given in Figure 4.3, sensitivity functions define the interplay between inputs (reference r, noise n, disturbance d) and outputs (process output y, control signal u and error e) of the system. These sensitivity functions, the output sensitivity function S, complementary sensitivity function T and the controller

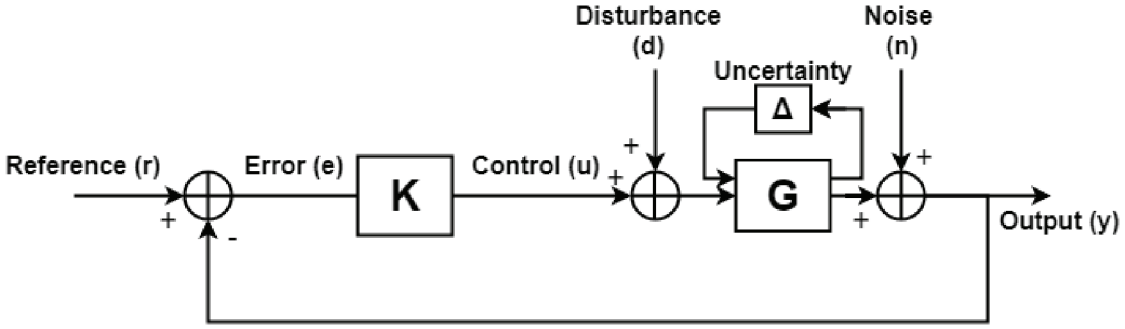

Figure 4.3. Feedback control loop with the output measurement noise, input/output disturbances and uncertainty in the plant model

sensitivity function KS are expressed as

$$S(s) = \frac{1}{1+GK} \tag{4.4}$$

$$T(s) = \frac{GK}{1+GK} \tag{4.5}$$

$$KS(s) = \frac{K}{1+GK} \tag{4.6}$$

Here, closed-loop transfer function is alternatively named as complementary sensitivity function since $S + T$ = 1. With these definitions, output y, control signal u and error e are expressed in Laplace domain as in 4.7, 4.8 and 4.9.

$$Y(s) = T(s)r + SG(s)d + S(s)n \tag{4.7}$$

$$E(s) = S(s)r - SG(s)d - S(s)n \tag{4.8}$$

$$U(s) = KS(s)r - T(s)d - KS(s)n \tag{4.9}$$

Frequency characteristics of these sensitivity functions, such as their peak gain and bandwidth, are adjusted to meet the performance and robustness requirements of the control. To minimize the tracking error e, gain of the sensitivity function S is desired

to be as small as possible. This yields to a good reference tracking performance of the closed-loop system. Additionally, to have a good level of noise attenuation in the output y and disturbance rejection in control signal u, T is desired to be small. Generally a small KS is preferred to minimize the effect of noise n on the control signal u. By knowing the characteristics of the actuator used in the control system, KS is minimized in the frequency range where the changes in reference r occurs, to prevent possible actuator saturation (Skogestad and Postletwaite, 1996). In addition to these, to minimize the effect of modeling uncertainties, T is desired to be small in frequencies where uncertainties are expected to occur (Bibel and Malyevac, 1992).

However, there are constraints for minimizing the sensitivity functions in the same frequency range. If one looks at the Equation (4.7), to have a good reference tracking performance, since S is desired to be small to minimize the error and $S + T = 1$, T should be close to 1. At the same time, to mitigate the effect of the parametric uncertainty on the output, T should be minimized. Thus, S and T cannot be minimized at the same time. Since the reference and disturbances occur at low frequencies, and noise & uncertainties are generally concentrated at high frequencies, S is minimized when $\omega \rightarrow 0$ and T is minimized when $\omega \rightarrow \infty$. This procedure is called as *loop shaping*.

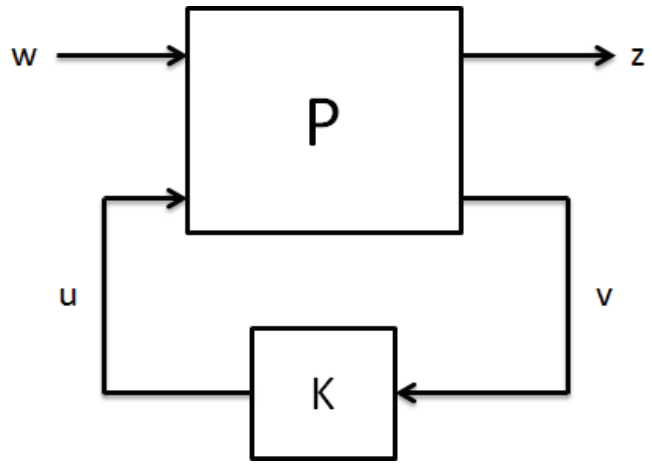

Figure 4.4. P-K structure of the H infinity control problem

To shape the sensitivity functions in desired way, the controller K is the key element. To find the controller K that satisfies the design requirements explained above for a more optimal and robust system, the H_∞ control problem is defined. The structure of the H_∞ control problem, or so-called P-K structure, is given in Figure 4.4. Here, w is the vector of exogenous inputs (reference, disturbance, noise), z is the vector of errors to be minimized, v is the vector of measurements (sensor outputs) and u is the vector of control

signals (Bansal and Sharma, 2013). P is the generalized plant, which has 2 inputs (w, u) and 2 outputs (z,v). The aim of the Robust H_∞ control is finding a controller K that generates a control signal u from the measurement data v to minimize the effect of inputs w on errors z. This is done by minimizing the H_∞ norm of the transfer function T_{zw} from w to z. Consequently, errors arising in the system can be minimized.

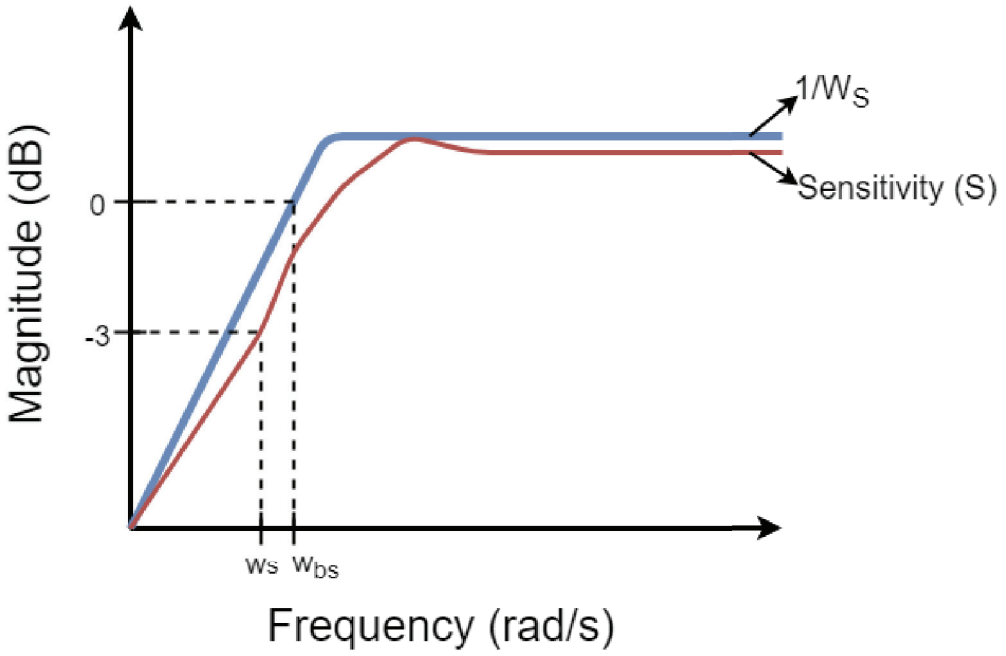

Figure 4.5. Ideal frequency responses for the sensitivity function and the inverse of the sensitivity weight

In the generalized plant P, weight functions that reflect the performance criteria for each sensitivity function mentioned above are included. They can be scalars, or type of low-pass & high-pass filters according to the needs for the controller design. Maximum & minimum gain and bandwidth of the weights are chosen to define an upper limit for each sensitivity function in frequency domain. Magnitude of the resulting closed-loop sensitivity functions should not exceed these limits defined by the multiplicative inverse of the weights ($1/W$), to guarantee the desired performance in terms of reference tracking, noise attenuation and disturbance rejection. As an example, sensitivity function S shows a high-pass behavior in an ideal system and treshold defined by the inverse of the sensitivity weight $1/W_S$ is shown in Figure 4.5. Additionally, possible modeling uncertainties, denoted as Δ, are defined for the system of interest, and possible perturbations G_p of the original plant G are found. In this way, the maximum relative error between the worst-case perturbed plant, which has the highest maximal gain among possible pertur-

bations, and the original plant is found as $|(G - G_p)/G|$. Maximal gain of the maximum relative error should be below the treshold represented by the inverse of the complementary sensitivity weight $(1/W_T)$ in the frequency range where uncertainties are expected to occur. Parameters of the weights should be well-defined to prevent instability due to the uncertainty and to meet the performance criteria at the same time, but if the chosen limits are too strict, an inadequate H_∞ controller might be obtained. With these weights, original plant G and controller K, the feedback structure in Figure 4.3 is manipulated as shown in Figure 4.6 (Bansal and Sharma, 2013; Nair, 2011) for the H_∞ controller design.

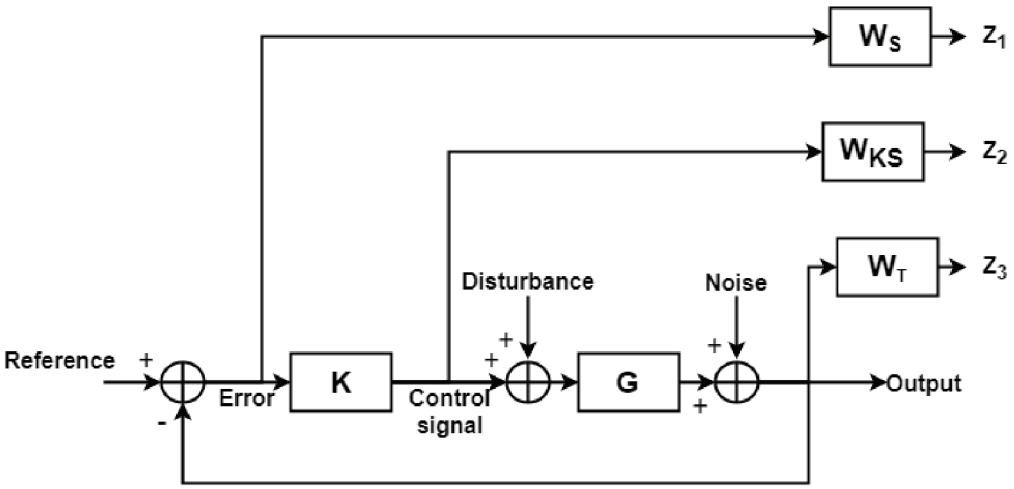

Figure 4.6. Manipulated structure of the feedback control loop for H infinity synthesis with weights

W_S is the sensitivity weight, W_{KS} is the control sensitivity weight and W_T is the complementary sensitivity weight. Here, new outputs z_1, z_2 and z_3 are defined as the controlled outputs, which are the weighted (shaped) versions of e, u and y in the sense of performance and robustness requirements. In some cases, instead of shaping all three sensitivity functions, only one or two sensitivity functions are weighted. It is decided by the designer according to the needs for the control. However, independent from how many weights are used, procedure for obtaining the H_∞ controller is the same. In general, the generalized plant matrix P is obtained from the original plant G, weights W and uncertainties Δ if any. General structure of an augmented plant matrix P and a closed-loop transfer matrix T_{zw}, which is obtained via *lower fractional transformation* from the P-K structure (Gu et al., 2005), in a H_∞ control problem are

$$P = \begin{bmatrix} P_{11} & P_{12} \\ P_{21} & P_{22} \end{bmatrix} \tag{4.10}$$

$$\begin{bmatrix} z \\ v \end{bmatrix} = \begin{bmatrix} P_{11} & P_{12} \\ P_{21} & P_{22} \end{bmatrix} \begin{bmatrix} w \\ u \end{bmatrix} \tag{4.11}$$

$$T_{zw}(s) = P_{11} + P_{12}K(I - P_{22}K)^{-1}P_{21} \tag{4.12}$$

As a result, T_{zw} takes the form in (4.13). Each element in T_{zw} reflects the control objective for a particular closed-loop sensitivity function. Thus, H_∞ optimal controller K is found to minimize the H_∞ norm of the transfer matrix, which is denoted as γ.

$$||T_{zw}||_\infty = \left\| \begin{matrix} W_S S \\ W_{KS} KS \\ W_T T \end{matrix} \right\|_\infty < \gamma \tag{4.13}$$

In the transfer matrix T_{zw}, magnitude of each transfer function T_{ij} from an input i to an output j is denoted as singular value σ_{ij}. Maximum singular value $\bar{\sigma}_{ij}$ is the maximum gain of the transfer function T_{ij} for this input & output pair over the whole frequency range. Thus, H_∞ norm of the transfer matrix T for a MIMO system is the greatest singular value of the system transfer matrix. In SISO systems, since there is a single closed-loop transfer function from a single input to a single output, H_∞ norm is identical to the maximal gain of the bode diagram of the closed-loop transfer function.

In this study, only the output sensitivity S and the complementary sensitivity T are shaped since there is no actuator constraint defined in the system. On the other hand, to see the level of the disturbance rejection, and noise attenuation for the control input u, frequency characteristics of the controller sensitivity KS in high frequencies and sensitivity & plant pair transfer function (SG) in low frequencies are checked after the design. Bode diagrams of the resulting sensitivity functions on frequency range ω are analyzed to see whether their magnitudes are below the treshold defined by the inverse of the weights ($1/W$), as given in the next Chapter. Weights used for the sensitivity (W_S) and the complementary sensitivity (W_T) are defined in this study as

$$W_S = \frac{\frac{s}{M_s} + \omega_{bs}}{s + \omega_{bs}\epsilon} \qquad S \leq 1/W_S \tag{4.14}$$

$$W_T = 1 \qquad T \leq 1/W_T \tag{4.15}$$

Thus, H_∞ control problem defined for this study has a form of

$$||T_{zw}||_\infty = \left\| \begin{matrix} W_S S \\ W_T T \end{matrix} \right\|_\infty < \gamma \tag{4.16}$$

Weight for the complementary sensitivity function is chosen as unity by looking at the maximum relative error of the possible uncertainties in the system. This is decided from the uncertainty scenarios that may possibly occur in a state-of-the-art HS-AFM system. Fluctuation in the parameters of the optical detection system, piezo, cantilever and controller are assumed to be negligibly small during the scan. Parameters of the cantilever used in the scan generally given in a range in the manufacturer in data-sheet, e.g., spring constant $0.2 < k < 0.3$, and user does not know the actual values. The range for the resonance frequency of the cantilever is small, but its spring constant k may shift by up to %50. Thus, the uncertainty in the state-of-the-art HS-AFM system model used in this study is defined as the uncertainty in the cantilever spring constant. It is observed that the maximum relative error occurs when the spring constant of the cantilever k decreases by %50. In this case, gain of the perturbed plant G_p is 2 times higher than the original plant G in the whole frequency range. Thus, the maximum relative error is 1 as $|G_p| = 2|G|$, and choosing the W_T as 1 guarantees that the relative error will be below the treshold defined by $1/W_T$.

M_s is the peak gain of the $1/W_S$, which defines an upper limit for the maximal gain of the sensitivity S. ω_{bs} is the crossover frequency, i.e., where $1/W_S$ crosses 1 (0 dB). ϵ is the gain of the $1/W_S$ when $\omega \to 0$. Since possible changes in the reference signal are mostly concentrated at low frequencies, minimizing ϵ yields to a small tracking error.

Here, M_s is chosen as 2 in every case to meet the maximum peak criterion, which states that to have a good modulus margin for safe operation, maximum gain of the sensitivity function S is desired to be below or equal to 2 (6 dB). Modulus margin is the minimum distance between the point (-1+0j) and the Nyquist plot of the loop gain, $L(jw) = G(jw)K(jw)$. Since the modulus margin $\Delta M = \dfrac{1}{|S_{max}|}$, keeping the maximal gain of S below 2 yields a modulus margin that is higher than 0.5. Since the Nyquist plot of the possible deviations $L_p(jw)$ of the loop gain in consequence of the uncertainty may pass from a closer distance to the point (-1+0j), the risk of instability due to uncertainties in the system can be decreased in this way.

ϵ is chosen to minimize the steady state-error and to improve the disturbance rejection performance, since minimizing the S minimizes the effect of disturbances on the system outputs. In this study, it is observed that choosing ϵ as 0.001 for each cantilever yields the best reference tracking performance. If it is decreased further, DC gain of the

resulting controller becomes higher than desired level and causes oscillations in its response. Thus, ϵ cannot be decreased any further to achieve better disturbance rejection, which is a tradeoff for shaping the sensitivity S in H_∞ design in this study.

Bandwidth of the closed-loop system is between the bandwidths of the sensitivity and the complementary sensitivity functions, i.e., $\omega_S < \omega < \omega_T$. Here, ω_S and ω_T are corner frequencies where sensitivity gains $|S(jw)|$ and $|T(jw)|$ cross 0.707 (-3 dB) in the frequency domain (Skogestad and Postletwaite, 1996). Thus, bandwidth of the weights chosen for the sensitivity and the complementary sensitivity define lower & upper limits for the closed-loop bandwidth. Since W_T is chosen as unity in this study, w_S is the main factor that adjusts the closed-loop bandwidth and thus, the closed-loop response speed. Bandwidths used for the sensitivity weight W_S for four cantilevers used in this study are given in Table 4.2. They are chosen to optimize the controllers to their most aggressive mode for each cantilever.

After defining the weights, obtaining the generalized plant P and resulting transfer matrix T_{zw}, H_∞ controller K can be found via analytical methods such as LMI approach (Coutinho et al., 2002) and algebraic Ricatti equations (Bansal and Sharma, 2013; Skogestad and Postletwaite, 1996). In this study, Robust Control Toolbox available in MATLAB is utilized for finding the H_∞ controller for each cantilever used in the state-of-the-art HS-AFM model. When the transfer functions of the plant G and weights W are defined, this toolbox enables synthesizing the H_∞ controller with very small computational errors. After the design, minimum achieved γ value is 25 for the cantilevers used in air, and 1 for the cantilevers in liquid. Their performance of topography acquisition in this study are analyzed in the next Chapter.

4.3. False Error Generation

In the state-of-the-art HS-AFM employed to scan soft biological specimen, set-point amplitude is chosen as close to the free-air amplitude, e.g. $0.9A_0$, to prevent strong interaction forces during the scan. Since the maximum scan speed is tried to be increased, controller bandwidths are adjusted to the highest possible level without causing instability in the closed-loop response. However, the error signal saturation phenomenon, which occurs when there is a dramatic fall or a downward step in the surface topography, is another factor that limits the maximum achievable scan rate. This especially occurs when the set-point is chosen as very close to the free-air amplitude in Dynamic-AFM. In this case, the maximum value that the error signal can reach is limited since the maximum

possible cantilever oscillation amplitude is equal to the free-air amplitude. Since the input of the controller is the error signal and the generated control signal is directly related to the level of error, this yields a slower response.

If the tip faces a downward step while tracing the surface, the tip-sample distance increases instantly and this condition minimizes tip-sample interaction forces. As a result, the oscillation amplitude starts to increase, and the error between the set-point and the current amplitude increases at the same time. However, since the maximum value that the error can reach is limited, speed of the compensation of this error is slow since the resulting controller response speed is slow. Thus, the tip cannot trace the surface accurately in this region, and it reaches the surface after a particular time period. This motion of the tip resembles a man with parachute who jumps off from the top of a hill. This phenomenon is called as *error signal saturation* (Sulchek et al., 2002) or the "parachuting effect".

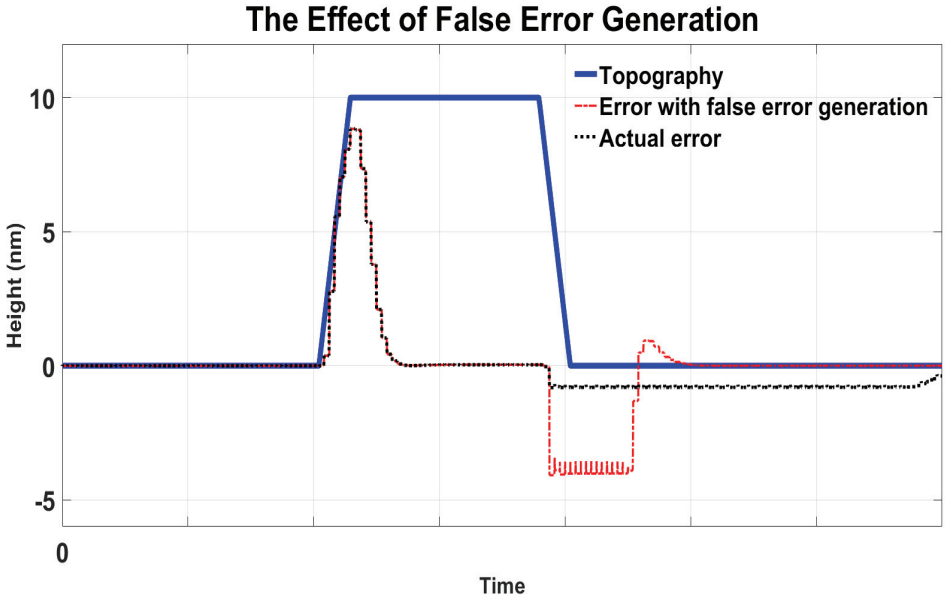

Figure 4.7. The change in error signal while tracing the topography

When the level of change in topography is very small, i.e., the tip-sample distance does not increase instantly during the scan, the effect of the error signal saturation observed on the controller response is neglectable. However, when there is a dramatic fall as seen in Figure 4.7, this becomes a remarkable problem that limits the scan rate. Features between the points where the falling edge starts and the point where the tip re-finds the surface inevitably missed due to this phenomenon if the scan rate is chosen as high. This can be prevented by lowering the set-point amplitude, since the level of maximum possi-

ble error increases and the effect of the error signal saturation is mitigated. However, this causes stronger interaction forces and it is not desired for imaging soft samples.

To minimize the error signal saturation, false error generation method is employed for the modeled state-of-the-art HS-AFM in this study (Balantekin and Degertekin, 2011). According to the false error generation method, lower and upper tresholds for the oscillation amplitude are defined. If the amplitude exceeds these limits, the error signal is amplified and added to the original error, and a false error is created. Resulting controller response becomes faster due to the increased (augmented) error signal, or "false error signal". Thus, the tip finds the surface in a shorter time. The response at the falling edge, consequently the obtained image, becomes more in accord with the original topography. The methodology is expressed as;

$$False\,error(t) = (A(t) - A_{upper}) \times G_{upper} + error(t) \quad if\ A(t) > A_{upper} \tag{4.17}$$

$$False\,error(t) = (A(t) - A_{lower}) \times G_{lower} + error(t) \quad if\ A(t) > A_{lower} \tag{4.18}$$

where A_{upper} and A_{lower} are the lower and higher tresholds, respectively. G_{upper} is the gain to amplify the error signal, and it is added to the original error to create the false error. These values are chosen carefully so as to prevent undesired defects in the controller response and strong tip-sample interaction forces when the tip finds the surface at the falling edge. Choosing the false error gain as very high may cause high level of oscillations or a negative overshoot in the actuation signal at the falling edge. The negative overshoot can be expressed as the case when the tip sinks to the sample surface at the point where the tip touches the surface. Thus, the balance between the response speed and resulting level of oscillations & negative overshoot at the falling edge while choosing the false error gain must be well-adjusted. To keep the level of oscillations and the negative overshoot in desired level, parachuting at the falling edge is allowed at a certain level. This is the tradeoff in false error generation method.

As it can be seen from the Figure 4.7, when the cantilever oscillation reaches the steady-state and its amplitude reaches the set-point amplitude, where the level of error signal is decreased to zero. When there is a topography change, the error increases at the beginning, and compensated by the controller after a while. If one looks at the falling edge of the topography, without the false error generation, the error signal increases to a some level but it is remarkably low compared to the rising edge. Thus, the controller

compensates this error very slowly, and the set-point is achieved again after a long period. With the contribution of the false error generation, the error is increased by couple of times at the falling edge, the tip re-finds the surface quicker and the set-point for the oscillation amplitude is reached in a shorter time period. Thus, the topography can be acquired more accurately at high scan rates.

Table 4.2. Parameters of the controllers chosen for each cantilever in different media

Cantilever Resonance Freqency (MHz)	**Medium**	**PI Controller**			**H_∞ Controller**	
		P gain (x 10^{-3})	I gain (x 10^{3})	False error gain	ω_b (krad/s)	False error gain
0.3	Air	40.5	2.4	6	0.08	3.8
5	Air	112.5	19.3	8	1.6	3.8
0.3	Liquid	450	40.5	2.3	1.1	6
1.2	Liquid	315	113	2.8	800	5

In this study, the lower treshold in (4.18) is not used since it has no significant effect on improving the scan rate. Since the set-point peak-to-peak amplitude is 9 nm, upper treshold is chosen as 9.1 nm. In order to choose false error gains G_{upper}, a methodology is defined such that the amplitude of oscillations or the level of the negative overshoot arise at the falling edge should not exceed %10 of the height of the topography with the selected gains. Since the PI and H_∞ controllers have different response speeds, the resulting level of oscillations and the negative overshoot depend on the response speed of the controller, different false error gains are chosen for them for each cantilever used in the system. It is observed that in order the satisfy the condition for choosing the false error gains, lower gains are required for H_∞ controller in air, and for PI controller in liquid. Chosen false error gains for PI and H_∞ controllers, together with controller parameters found for each cantilever is given in Table 4.2.

CHAPTER 5

RESULTS AND DISCUSSION

To test the performance of the modeled state-of-the-art HS-AFM system in topography acquisition with PI and H_∞ controllers, a sample to be scanned is defined such that a single feature on this defined sample is composed of a rectangular pulse, whose height is 10 nm, and a flat region whose height is 0. This definition is made according to the mean height observed in biological samples (DNA, proteins, etc.). Rising and falling edges are taken as a ramp, whose width are %10 of the total width of the pulse. There are 10 identical features like this on a single line (in fast-scan axis), and there are 100 identical lines in parallel in a frame (in slow-scan axis). Defined feature topography is modeled as an input signal to the system model in SIMULINK, thus its length varies due to the simulation time. Since the time required to scan the sample topography depends on the scan rate in a real-time AFM and HS-AFM, simulation time represents the scan rate and thus, the acquisition time for a single feature. By knowing the acquisition time of a single feature and the complete waveform of the sample topography in a frame, achieved frame rate with the used controller is calculated for each cantilever.

Simulations are performed in four different cases; in ideal conditions, with the measurement noise, with %50 parametric uncertainty in the spring constant of the cantilever, and with a disturbance which consists of a single impulse-like pulse, as preferred in disturbance rejection analysis for controllers (Hyvamaki, 2008). Measurement noise is modeled as white noise in SIMULINK whose rms value is 0.1 nm, representing the total noise that arises in the system. In practice, the noise observed in a conventional AFM and the state-of-the-art HS-AFM is indeed a type of Gaussian white noise whose rms value is around 1 Angstrom (0.1 nm). Thus, modeling of noise in this study reflects the one in the physical system. In addition, for the disturbance rejection analysis of the system with each controller in the modeled state-of-the-art HS-AFM, the original topography is replaced by a pulse whose width is equal to the duration of 2 cycles of the cantilever oscillation (2-taps). Its height is taken as 10 times the height of the original topography (100 nm). This model of disturbance represents an instant, unexpected dramatic change in the sample topography. Therefore, responses of controllers to this dramatic change are observed. Furthermore, to model the parametric uncertainty, the spring constant of the cantilever in the HS-AFM model is decreased by %50 without changing the controllers

and the other parameters for each cantilever used in the state-of-the-art HS-AFM model. Simulations are performed, and results obtained for four cases are compared. Additionally, bode magnitudes of the frequency responses of closed-loop sensitivity functions, and transfer functions from the error to the actuation signal (Z-actuation) are given. Obtained results are analyzed in sections that are dedicated to each cantilever.

As mentioned before, the maximum scan rate for an AFM and HS-AFM depends on the capability of Z-feedback and X-Y scanners in AFM. Since the performances of PI and H_∞ controllers in Z-feedback are investigated in this study, X-Y scanners are taken as ideal and maximum scan rate is found from the capability of Z-actuation with each controller. Maximum frame rate is obtained from the minimum achieved acquisition time, number of features per line, and number of lines per frame. Since the acquisition time depends on the simulated scan time in the defined feature topography in SIMULINK, the minimum acquisition is decided by lowering the simulation time and observing the level of corruption in the control signal. Here, a methodology is defined in this study such that in the minimum acquisition time for the used controller, before the tip reaches the falling edge of the defined feature during the scan, height of the control signal provided by this controller reaches at least %90 of the height of the original topography. It is checked for PI and H_∞ controllers, and it is found that for each cantilever, PI is slower and its response reaches to the %90 of the topography after the H_∞ response already reaches this level. Thus, the achievable minimum acquisition time with H_∞ controller is shorter than PI in this manner. However, the comparison is done in a different manner. Since the PI response is slower than the H_∞ response, the simulations for comparing the performances of controllers in topography acquisition in ideal conditions, and their robustness in response to exogenous effects (noise, parametric uncertainty), are performed in the minimum acquisition time of PI controller except for their disturbance rejection analysis. As the waveform of the used disturbance model is different than the original topography, a different time scale is preferred in these simulations to see the time period for the tip to re-find the surface with both controllers.

In ideal conditions, the time scale used for the simulation, which is the minimum acquisition time with PI controller, is simply expressed as the minimum acquisition time per feature in the system. In this case, the error between the control signal, and the original feature topography is calculated for each cantilever for both PI and H_∞ controllers by using the formula (Balantekin and Degertekin, 2011) as

$$acquisition\ error = \frac{\int |controller\ response - sample\ topography|}{\int |sample\ topography|} \times 100\% \quad (5.1)$$

It is observed that the level of percentage acquisition error obtained with H_∞ controller remarkably lower than the one with PI for three cantilevers except the regular low-frequency cantilever used in air. For this cantilever, the obtained error is slightly less with PI but the difference between PI and H_∞ acquisition errors is minimal. Furthermore, in ideal conditions, the minimum acquisition time required for H_∞ controller to yield the same acquisition error obtained for PI is also found for each cantilever. By knowing the minimum acquisition time for a single line scan with both controllers, the complete acquisition time of the frame is found. Thus, the maximum number of frames that can be obtained in a second, i.e., frames per second (fps), is found for PI and H_∞ controllers for each cantilever by using the minimum acquisition time they yield. The minimum acquisition time, the frame rate and the error in acquired topography with PI and H_∞ controllers are given in Table 5.1, along with the minimum acquisition time and the frame rate achieved with H_∞ controller for the same level of error. As it can be seen, with the same allowed acquisition error, the frame rate can be increased up to 2 times with H_∞ controller compared to the PI, except for the low-frequency cantilever in air.

Table 5.1. Acquisition Time, Rate and Error obtained for each cantilever in different media

Cantilever Resonance Freqency (MHz)	**Medium**	**Min. acquisition time per feature (μs)**	**Frame rate (fps)**	**Error in acquired topography (%)**		**Min. acquisition time with H_∞ controller (μs)**	**Frame rate with H_∞ controller (fps)**
				PI Cont.	H_∞ Cont.		
0.3	Air	4000	0.25	74	78	4076	0.25
5	Air	400	2.5	46	31	216	4.6
0.3	Liquid	400	2.5	61	29	295	3.4
1.2	Liquid	140	7.1	61	25	70	14.3

5.1. Low Frequency Cantilever in Air

Frequency responses of the closed-loop sensitivity functions for the regular low-frequency cantilever used in air, shown in Figure 5.1, indicate that the design goals that are defined via multiplicative inverse of the weights $(1/W)$ are achieved in Robust H_∞

controller design. It is observed that the magnitude of the resulting sensitivity (S) and the complementary sensitivity (T) functions are below the treshold ($1/W$) for both PI and H_∞ controllers. However, frequency characteristics of the sensitivities for two controllers are different at particular frequencies. At low frequencies, i.e., when $\omega \rightarrow 0$, gain of the sensitivity function and thus, the sensitivity & plant pair (SG) obtained for PI controller are lower than the ones obtained for the H_∞ controller. This is caused by the integrator of the PI controller. Theoretically, this yields to a lower steady-state error and a better low-frequency disturbance rejection performance, but the false error gains are also effective in the time-domain performance. Thus, even though the sensitivities give an idea for the time-domain performance, simulation results may differ from the expectations that is deduced from the sensitivity functions.

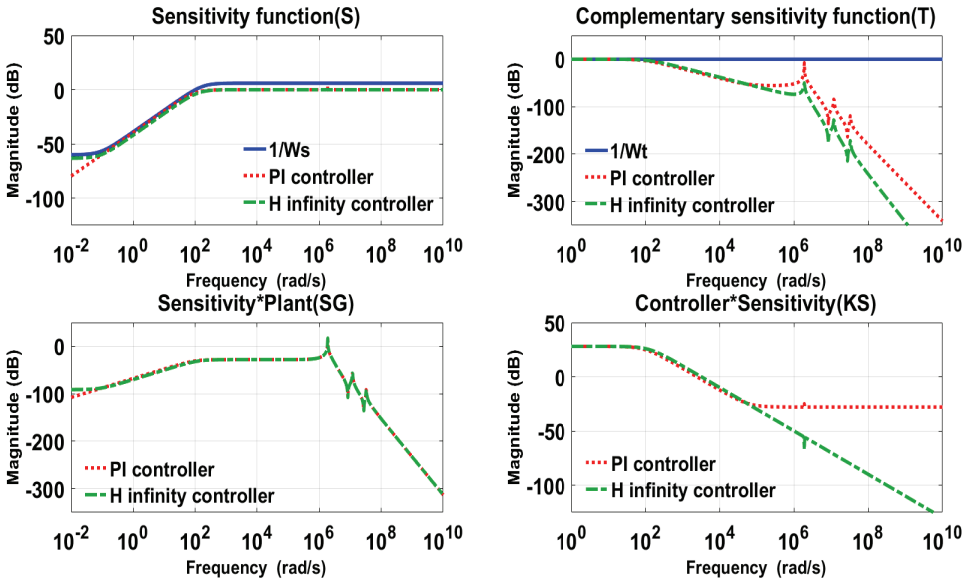

Figure 5.1. Magnitudes of the closed-loop sensitivity functions achieved for the low frequency cantilever in air

It is observed that the gains of the three resonance frequencies, which are shown as peaks in the complementary sensitivity, are higher for the PI controller case. This indicates that the risk of instability in the closed-loop response due to the parametric uncertainty is higher with the PI controller. Additionally, the gain of the controller sensitivity function KS cannot be minimized at high frequencies by using the PI controller, and the effect of high-frequency noise is expected to be higher on the control signal. Since the control signal is used to obtain the sample image, the resulting image becomes more noisy.

Along with the closed-loop sensitivities, the frequency response of Z-actuation transfer function from the error to the actuator signal, which is composed of the controller and the Z-piezo, are investigated as given in Figure 5.2. It is observed that the DC gain of the Z-actuation for the PI controller is larger than the one for the H_∞ controller. Additionally, the gain of this transfer function for PI controller is also higher when $\omega \rightarrow \infty$. Phase response of the Z-actuation shows that the actuator response is in phase with the error signal with H_∞ controller at low frequencies, although 90 degrees of phase lag occurs for the PI controller in the same frequency range. However, at high frequencies, PI controller yields a better phase response in Z-actuation.

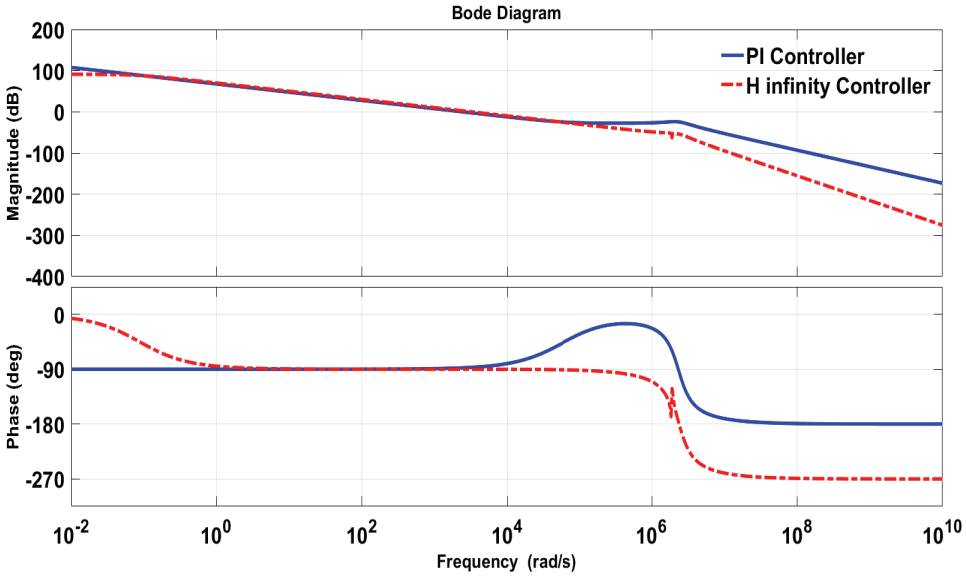

Figure 5.2. Bode plots of the Z-actuation transfer function from error signal to the actuator signal for the low frequency cantilever in air

Simulation results which are performed in ideal conditions and with noise, disturbance and uncertainty for the low-frequency cantilever in air are given in Figure 5.3. Even though the speed of actuation with H_∞ controller is faster than the one with PI at rising edge of the feature, the acquisition error that H_∞ controller yields is slightly higher as its response is slower in falling edge due to adjusted false error gains. It is seen that, in this state, the level of oscillations in the responses obtained with PI and H_∞ controllers are below 1 nm at the falling edge, and the condition for choosing the false error gains is satisfied. H_∞ controller shows a better performance under the effect of noise as it can be seen from the Figure 5.3(b). Thus, the result expected from the frequency response of the KS in Figure 5.1 is obtained.

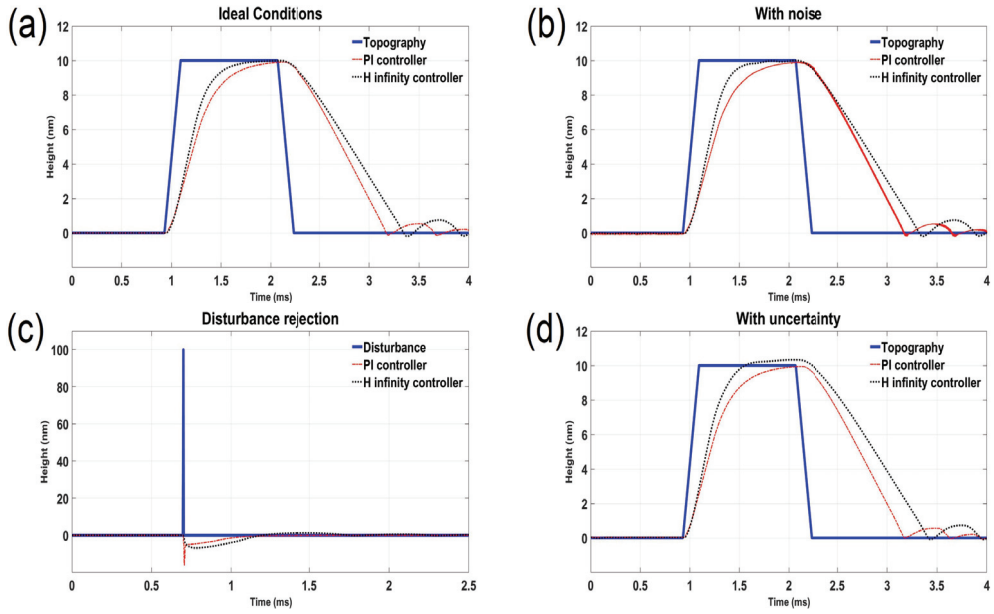

Figure 5.3. Actuator responses with PI and H_∞ controllers versus the sample topography after the simulation in a) Ideal conditions b) with the measurement noise c) with disturbance d) with parametric uncertainty in cantilever spring constant k, for the low frequency cantilever in air

As expected from the magnitudes of S and SG at low frequencies, disturbance rejection is slightly better with PI controller for this cantilever. However, there is no significant difference between the disturbance rejection performances of the system with two controllers for this cantilever, as it is seen from Figure 5.3(c). Furthermore, %50 of decrease in the spring constant of the cantilever gives rise to a condition that the tip enters the attractive region at the top of the topography, as given in Figure 5.3(d). In this situation, the tip does not touch the sample and oscillates above the surface with the set-point amplitude, and only the attractive Van der Waals forces are in action. This is due to the bi-stable phenomenon observed in tapping-mode AFM as explained in Section 3.2. The effect is observed clearly in the simulation that are performed in air environment. Since H_∞ controller yields a quicker response in Z-actuation, the tip enters to the attractive region before the falling edge, although the actuator response with PI controller cannot reach this level as it is slower. In order to see this effect in PI response, the scan rate must be decreased by extending the simulation time. It is also observed that this phenomena is valid not only for the scan in air, but also for the scan in liquid. However, in order to observe this effect in liquid, the uncertainty level should be increased, e.g., up to %80, which is not quite realistic. In addition, level of oscillations in the PI response at the falling edge increases for a slight amount although there is no change observed in

the H_∞ response. Except for this, there is no corruption, e.g., ringings, instability, etc., observed in the actuator responses for both controllers. Thus, it can be said that the effect of parametric uncertainty is minimal in topography acquisition for both controllers for this cantilever.

5.2. Low frequency Cantilever in Liquid

Since the quality factor of the cantilever used in liquid is generally in the range of 1-3, actuation performance is better as the effect of error signal saturation is lower. Again, as given in Figure 5.4, bandwidth of the sensitivity function ω_s, which defines the closed-loop bandwidth of Z-feedback, is slightly higher with H_∞ controller.

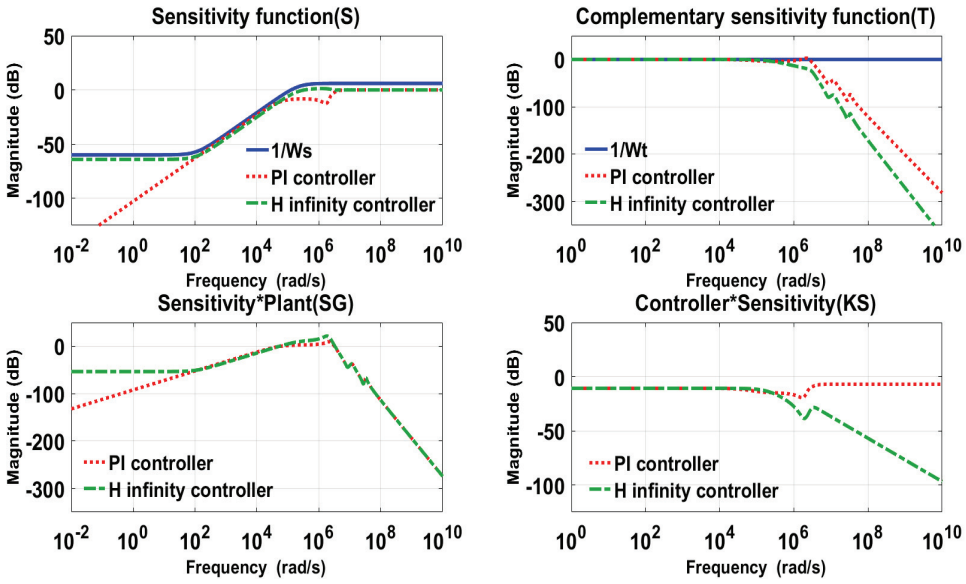

Figure 5.4. Magnitudes of the closed-loop sensitivity functions achieved for the low frequency cantilever in liquid

Like the previous case, gain of the sensitivity function S and SG in low frequencies is lower with PI controller. Maximal gain of the complementary sensitivity T of the system in eigenmodes with PI controller is higher than the one with H_∞ controller, which causes a higher risk of instability due to uncertainties since the robust performance criterion for the system is represented by the treshold $1/W_T$. Furthermore, as it can be seen from the frequency response of the controller sensitivity, gain of KS does not go to 0 with PI controller at high frequencies. Conversely, the gain of KS is higher than the gain at low frequencies for this case. However, like the controller sensitivity behavior in

previous case, gain of KS gradually decreases with H_∞ controller when $\omega \to \infty$. Thus, noise is expected to affect the control signal less with this controller.

Bode diagrams of the Z-actuation for two controllers show that the gain of the Z-actuation with PI controller is higher than the one with H_∞ controller when ω <100 rad/s and $\omega \to \infty$, as in the previous case. Additionally, phase response of the Z-actuation with H_∞ controller is better when ω <100 although the one with PI controller has a lower phase lag at high frequencies.

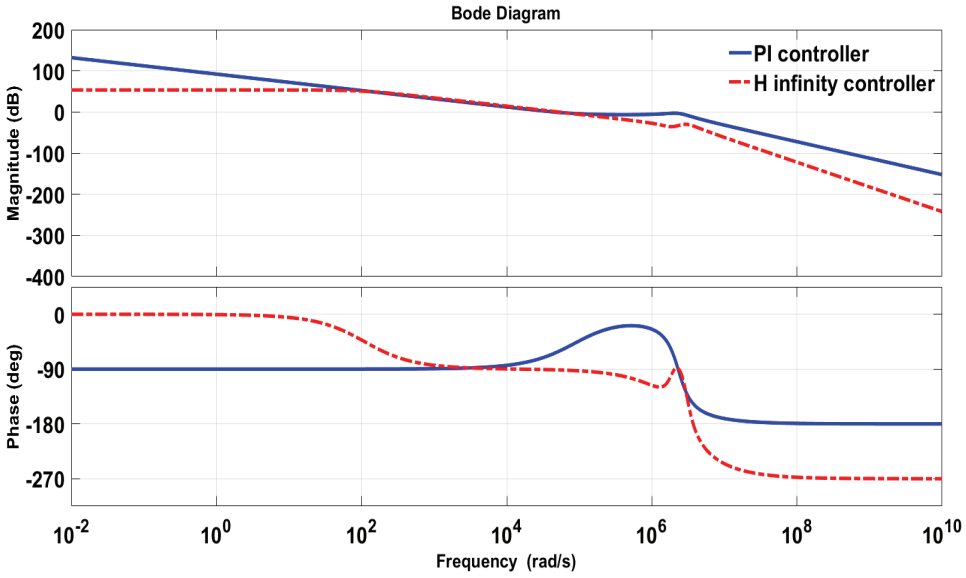

Figure 5.5. Bode plots of the Z-actuation transfer function from error signal to the actuator signal for the low frequency cantilever in liquid

Simulation results for this cantilever is given in Figure 5.6. Response speed of the H_∞ controller is remarkably higher than the one with PI controller, as it is seen from the Figure 5.6(a). In the minimum acquisition time of the PI controller, topography is almost completely captured with H_∞ controller. Its response is almost ideal except the delay caused by the peak detector at the rising edge. This yields a lower acquisition error compared to the one with PI controller. In contrast to the simulation result in air environment, response of the H_∞ controller does not oscillate at the falling edge although PI yields a similar response to the previous case. Thus, the false error gain of the H_∞ controller is chosen from a different aspect, i.e., the negative overshoot at the point where the tip finds the surface. In this case, the gain is chosen such that the peak amplitude of the negative overshoot should not exceed the %10 of the total height of the topography (1 nm). As it is seen from Figure 5.6(a), overshoot is below this treshold.

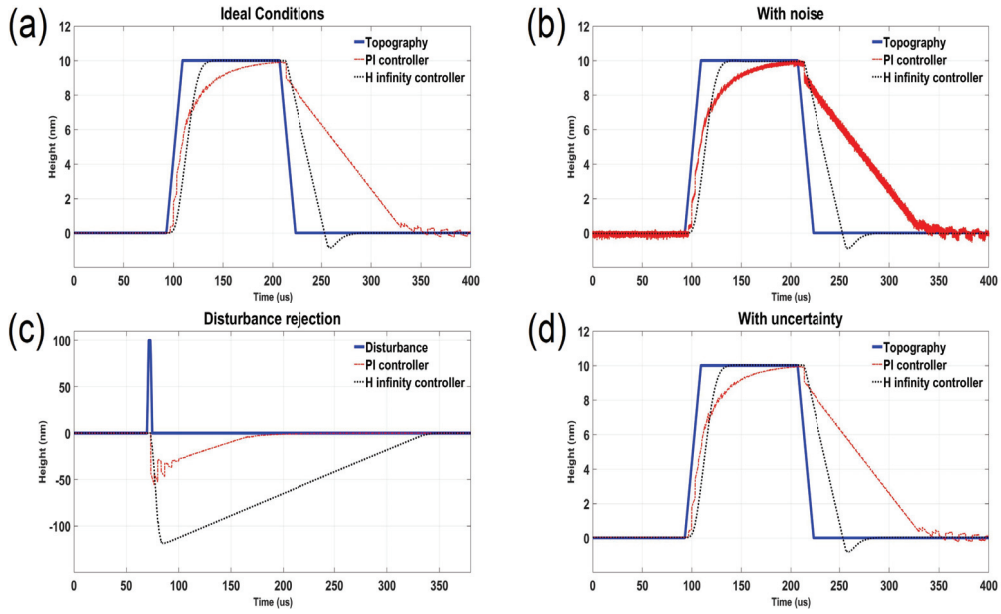

Figure 5.6. Actuator responses with PI and H_∞ controllers versus the sample topography after the simulation in a) Ideal conditions b) with the measurement noise c) with disturbance d) with parametric uncertainty in cantilever spring constant k, for the low frequency cantilever in liquid

Compared to the previous case, the effect of noise on PI response is more pronounced as it can be seen from Figure 5.6(b). H_∞ controller is not affected from the output measurement noise and yields an ideal response. This means that in a realistic system with the presence of noise, a more quality image can be obtained with H_∞ controller. On the other hand, disturbance rejection performance of the PI controller is way better for this cantilever, as shown in Figure 5.6(c). Thus, despite the contribution of the false error generation, the result expected from the characteristics of S and SG at low frequencies is observed here. Finally, if one looks at the result with uncertainty, there is almost no change in responses except small differences compared to the ideal conditions as in the previous case. Level of oscillations in PI response slightly increases although there is no change with H_∞ controller.

5.3. High Frequency Cantilever in Air

In the simulation carried out for the high-frequency cantilever in air environment, the difference between achieved bandwidths for PI and H_∞ controllers are more than other cases, as it is shown in the frequency responses of the sensitivity functions in Figure 5.7.

Except for this, the closed-loop sensitivities and frequency responses of Z-actuation for two controllers show similar behaviors of previous cases.

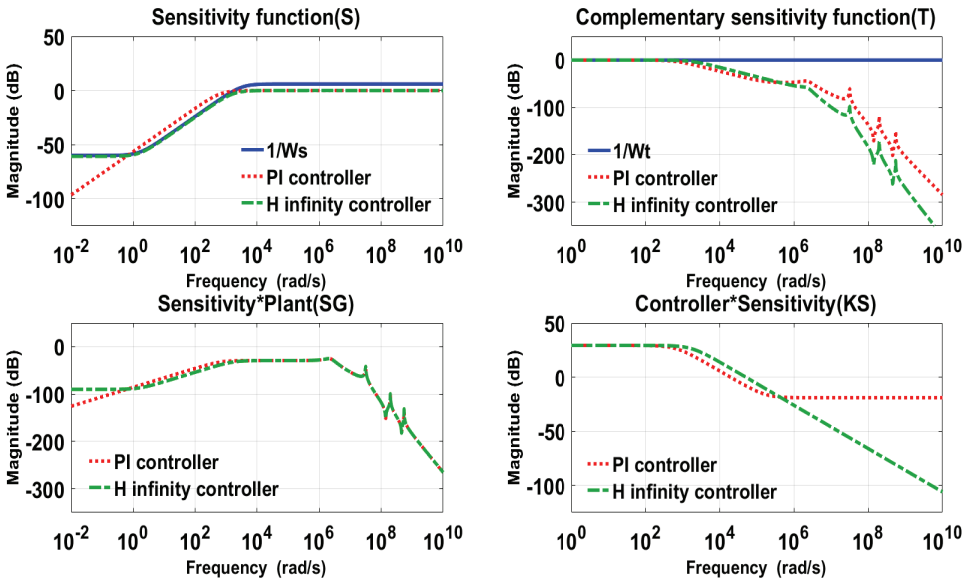

Figure 5.7. Magnitude of the closed-loop sensitivity functions achieved for the high frequency cantilever in air

Gain of T in three eigenmodes is optimized to a lower level with H_∞ controller in comparison to the PI controller. Additionally, the gain of KS goes to -∞ when $\omega \rightarrow \infty$ with H_∞ controller although it remains at a constant level with PI. Furthermore, gain of S and SG with H_∞ controller is lower than ones with the PI controller in low frequencies. Meanwhile, as it can be seen from Figure 5.8, DC gain of the Z-actuation with H_∞ controller is again lower than the one with PI controller in high frequencies. Phase response of the Z-actuation obtained with H_∞ controller is better at low frequencies. At high frequencies, the result is similar to the previous cases, i.e., the phase is 90 degrees lower with H_∞ when $\omega \rightarrow \infty$.

Response of the H_∞ controller is faster than the PI response due to its higher bandwidth, and topography is almost completely acquired except at the falling edge when the simulation is performed in the minimum acquisition time for the PI controller. Thus, in ideal conditions, H_∞ has an absolute superiority in topography imaging, as the percentage error it yields is 2 times lower compared to the PI. Due to the characteristics of KS at high frequencies, response of the PI becomes noisy although the response of H_∞ controller remains almost the same, as it is shown in Figure 5.9(b).

In contrast to the previous cases, disturbance rejection performance of the H_∞

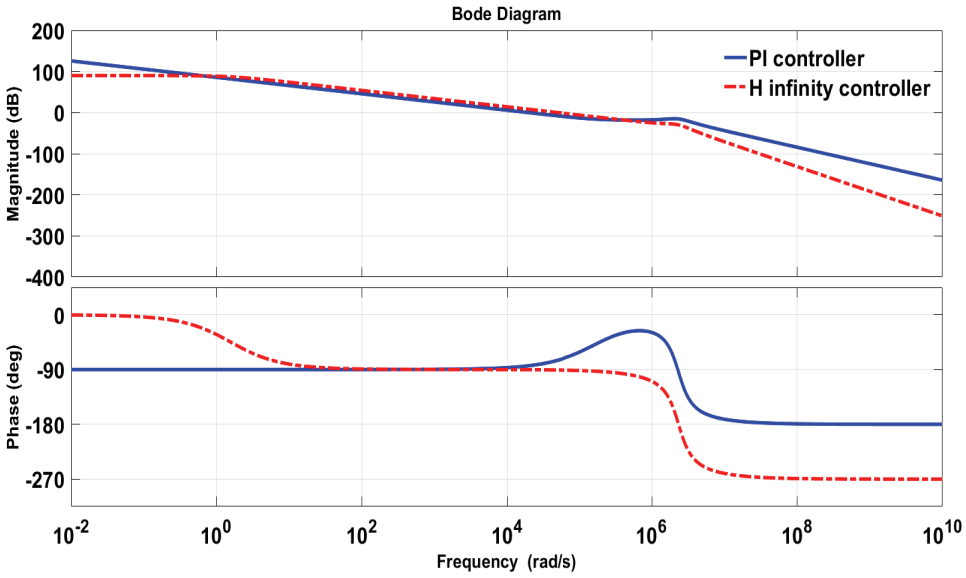

Figure 5.8. Bode plots of the Z-actuation transfer function from error signal to the actuator signal for the high frequency cantilever in air

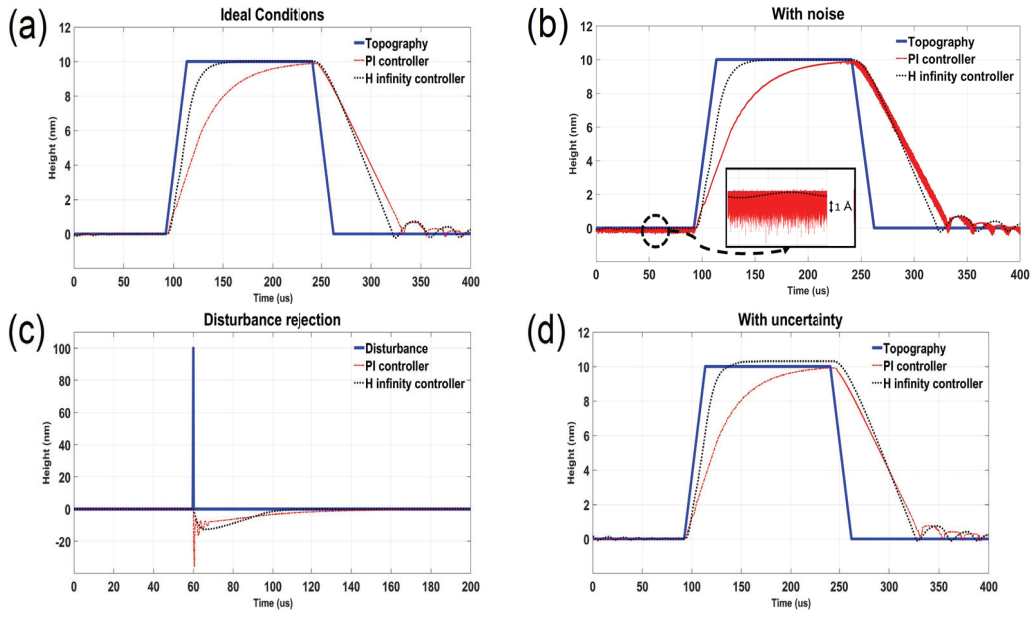

Figure 5.9. Actuator responses with PI and H_∞ controllers versus the sample topography after the simulation in a) Ideal conditions b) with the measurement noise c) with disturbance d) with parametric uncertainty in cantilever spring constant k, for the high frequency cantilever in air

controller is slightly better than PI, but, the difference is minimal. Thus, it is observed that the contribution of the false error yields a different result than expected from the sensitivity functions (see Table 4.2). Furthermore, as mentioned before, when the spring constant of cantilever decreases by %50 (uncertainty), tip stays in the attractive region with H_∞ controller at the top of the topography as in the first case, since the scan is performed in air. Additionally, height of the PI response reaches to the original height of the topography rather than the level of %90, but it does not enter the attractive region before the falling edge as its response is slower. Thus, at the maximum scan rate achievable with the PI controller, the topography image can be obtained more accurately with H_∞ controller in ideal conditions and in the presence of exogenous effects.

5.4. High Frequency Cantilever in Liquid

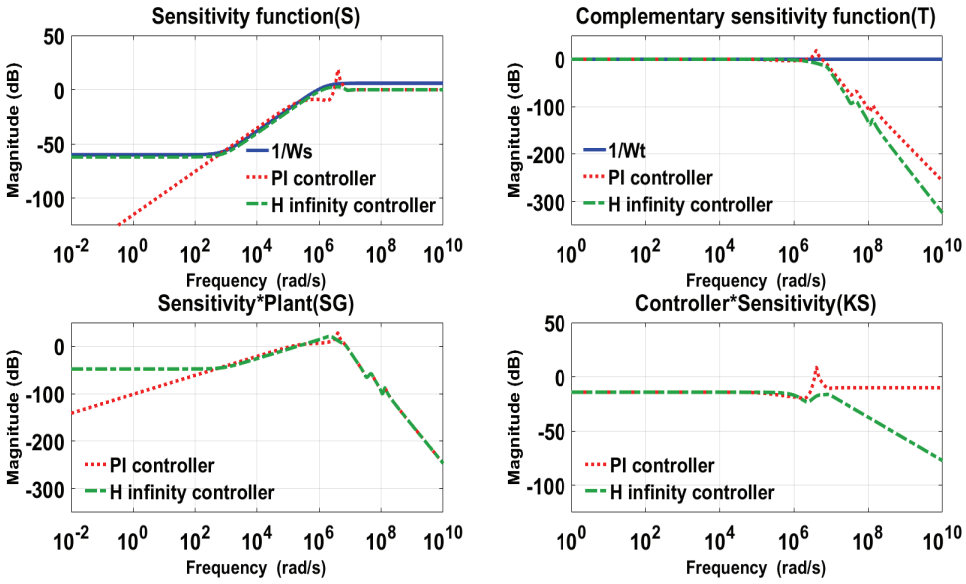

Figure 5.10. Magnitude of the closed-loop sensitivity functions achieved for the high frequency cantilever in liquid

Highest closed-loop bandwidths are achieved with both PI and H_∞ controllers for the high frequency cantilever in liquid, as shown in Figure 5.10. Even though the cantilever having highest resonance frequency is the one used in the previous case, the small quality factor in liquid enables a faster scan compared to the one in air environment. Here, magnitude of the closed-loop sensitivities obtained with PI controller exceed the limits provided by the multiplicative inverse of the weights at the resonance frequency of

the 1st eigenmode. Additionally, gain of three flexural eigenmodes are lower with H_∞ controller as in three previous cases, which yields a lower risk of instability due to the parametric uncertainty. Like the previous cases, KS is lower at high frequencies for H_∞ controller, resulting in a better noise attenuation in control signal. Finally, the PI controller minimizes the magnitude of the sensitivity S and SG when $\omega \rightarrow 0$, which indicates a better disturbance rejection.

The difference between Z-actuation transfer functions obtained for PI and H_∞ controllers is similar to the previous cases. Gain of the Z-actuation with PI is higher at low frequencies and when $\omega \rightarrow \infty$. Error signal (input) is in phase with the actuator response with H_∞ when $\omega < 100$ rad/s. At high frequencies, actuator response with the PI controller becomes 90 degrees ahead the one with H_∞ controller.

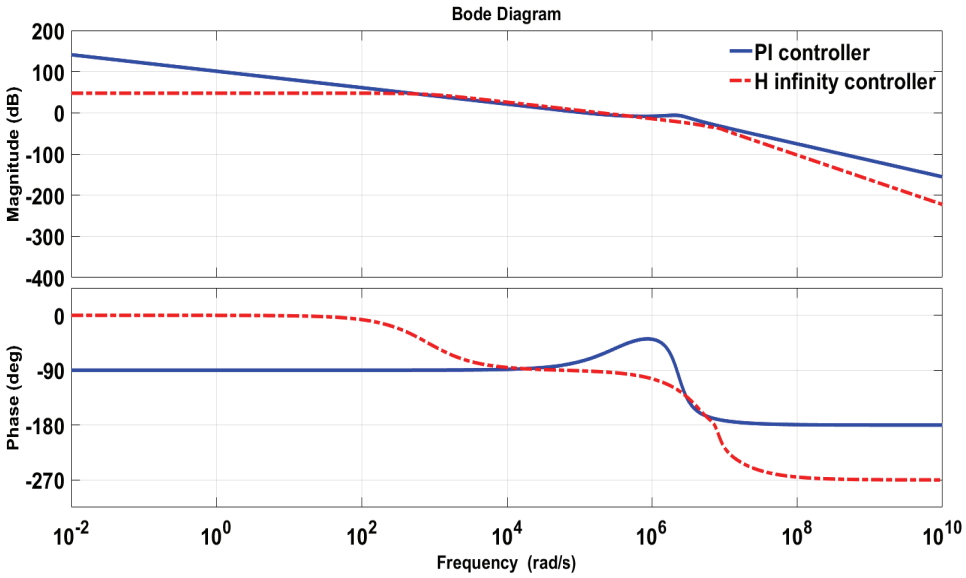

Figure 5.11. Bode plots of the Z-actuation transfer function from error signal to the actuator signal for the high frequency cantilever in liquid

The simulation results reflect the expected behavior obtained from the closed-loop sensitivity functions except small differences like the other three cases. As the bandwidth of the H_∞ controller is higher than the PI controller, and the phase lag it yields is lower at low frequencies, the tip traces the topography more accurately at high scan rates with this controller. Furthermore, under the effect of the measurement noise, resulting PI response becomes noisy but the one H_∞ remains the same and there is no deterioration in its response. Parametric uncertainty is also ineffective on H_∞ response, although it increases the level of oscillations in the PI response at the falling edge by a slight amount. However,

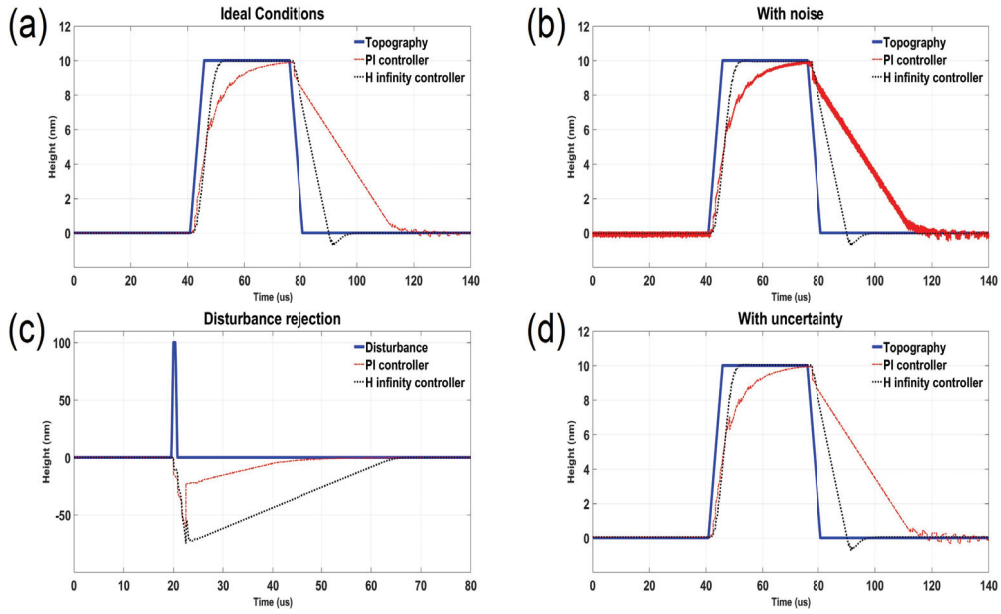

Figure 5.12. Actuator responses with PI and H_∞ controllers versus the sample topography after the simulation in a) Ideal conditions b) with the measurement noise c) with disturbance d) with parametric uncertainty in cantilever spring constant k, for the high frequency cantilever in liquid

disturbance rejection performance of the system with PI is better than the one with H_∞ controller, as shown in Figure 5.12(c). Thus, it can be said that PI has an advantage for disturbance rejection but H_∞ has a definite superiority in imaging performance in ideal conditions and under the effect of noise and uncertainty. As it is seen from Table 5.1, achieved frame rate with H_∞ controller is 2 times the frame rate with PI controller with the same level of error. It can be clearly seen from the result obtained in ideal conditions shown in Figure 5.12(a). This is the most remarkable difference observed in controller performances in Z-feedback among four cases. As the cantilever used in this simulation is the same as the one used in Ando's state-of-the-art HS-AFM, this result shows the clear advantage of using the H_∞ controller in state-of-the-art HS-AFM.

CHAPTER 6

CONCLUSION AND OUTLOOK

In this study, it is observed whether it is worth to use the Robust H_∞ controller on behalf of the typically used PI controller to improve the scan rate further in the state-of-the-art HS-AFM. Four different cantilevers, regular low-frequency cantilevers and small high-frequency cantilevers to be employed in air and liquid media, are simulated in MATLAB/SIMULINK environment.. These cantilevers are modeled with their first three flexural eigenmodes, along with the amplitude detector, Z-piezo, controller, false error generation and tip-sample interaction forces. Thus, differently from the other studies that try to observe the effect of H_∞ control in AFM and HS-AFM, the controller effect is studied for four different cantilevers used in the state-of-the-art HS-AFM, operated in both air and liquid, in ideal conditions, and with noise, disturbance and uncertainty separately.

It is found that for the low-frequency cantilever in air, the difference between PI and H_∞ controller responses is marginal. For the low frequency cantilever in liquid, H_∞ controller has an enhanced performance in topography acquisition and in noise attenuation. On the other hand, PI is better in disturbance rejection. For the high-frequency cantilever in air, H_∞ controller yields a 2 times lower percentage acquisition error in the minimum acquisition time of the PI controller. In this case, H_∞ shows a better performance under the effect of all exogenous effects. Most remarkable results are obtained for the high-frequency cantilever in liquid, the state-of-the-art HS-AFM system in this case can be operated 2 times faster with H_∞ controller compared to the PI controller with the same level of acquisition error. For this cantilever, PI is again better in disturbance rejection but H_∞ has a more quality response in noisy condition.

The state-of-the-art HS-AFM model developed in this study can be further improved by including the models of dither piezo and quadrant photodiode. Moreover, nonlinear dynamics of the piezos in the system (dither and Z-piezos), such as hysteresis, creep, structural vibrations and cross-couplings between X-Y scanners and Z-piezo can be included in the model. By including these phenomena, the system model can be made more realistic.

In addition to these, this study can be extended by implementing the designed H_∞ controller on an FPGA. In this way, the experiments can be carried out in a physical system, and obtained results can be compared to the ones obtained in this thesis. Further-

more, different control approaches other than robust nonlinear H_∞ controller used in the study can be studied in the modeled state-of-the-art HS-AFM, such as adaptive control, lead/lag compensators, LQG/LQR control or model predictive control. These controllers can also be implemented in a real-time system.

REFERENCES

Ando, T. (2012). High-speed atomic force microscopy coming of age. *Nanotechnology 23*(6), 062001.

Ando, T. (2013). Molecular machines directly observed by high-speed atomic force microscopy. *FEBS Letters 587*, 997–1007.

Ando, T. (2014). High-speed afm imaging. *Current Opinion in Structural Biology 28*, 63–68.

Balantekin, M. (2015). High-speed dynamic atomic force microscopy by using a q-controlled cantilever eigenmode as an actuator. *Ultramicroscopy 149*, 45–50.

Balantekin, M. and A. Atalar (2003). Simulations of switching vibrating cantilever in atomic force microscopy. *Applied Surface Science 205*, 86–96.

Balantekin, M. and M. L. Degertekin (2011). Optimizing the driving scheme of a self-actuated atomic force microscope probe for high-speed applications. *Ultramicroscopy 111*, 1388–1394.

Bansal, A. and V. Sharma (2013). Design and analysis of robust h-infinity controller. *National Conference on Emerging Trends in Electrical, Instrumentation and Communication Engineering (IISTE) 3*(2).

Barzanilla, M., B. Drake, E. Nudler, M. Kashlev, P. K. Hansma, and H. G. Hansma (1994). Motion and enzymatic degredation of dna in the atomic force microscope. *Biophysical Journal 67*, 2454–2459.

benmoshe.net (2017). http://http://benmoshe.net/il/2017/03/05/. *(Accessed: June 6, 2018)*.

Bibel, J. E. and D. S. Malyevac (1992). Guidelines for the selection of weighting functions for h-infinity control. *Naval Surface Warfare Center*.

Binnig, G., C. F. Quate, and C. Gerber (1986). Atomic force microscope. *Physical*

Review Letters 56(9).

Brezina, L. and T. Brezina (2011). H-infinity controller design for a dc motor model with uncertain parameters. *Engineering Mechanics 18*(5), 271–279.

Chuang, N., I. R. Petersen, and H. R. Pota (2013). Robust h infinity control in fast atomic force microscopy. *Asian Journal of Control 15*(3), 872–887.

Coutinho, D. F., A. Trofino, and M. Fu (2002). Nonlinear h-infinity control: An lmi approach. In *15th Triennial World Congress*.

Garcia, R. and P. Perez (2002). Dynamic atomic force microscopy methods. *Surface Science Reports 47*, 197–301.

Gu, D. W., P. H. Petkov, and M. M. Konstantinov (2005). *Robust Control Design with MATLAB*. Springer.

Guthold, M., M. Bezanilla, D. A. Erie, B. Jenkins, H. G. Hansma, and C. Bustamante (1994). Following the assembly of rna polymerase-dna complexes in aqueous solutions with the scanning force microscope. *Proceedings of the National Academy of Sciences of the United States of America 91*(26), 12927 – 12931.

Guthold, M., X. Zhu, C. Rivetti, G. Yang, N. H. Thomson, S. Kasas, H. G. Hansma, B. Smith, P. K. Hansma, and C. Bustamante (1999). Direct observation of one-dimensional diffusion and transcription by escherichia coli rna polymerase. *Biophysical Journal 77*(4), 2284–2294.

Hansma, P., G. Schitter, G. E. Fantner, and C. Prater (2006). High-speed atomic force microscopy. *Science 314*(5799), 601–602.

Humphris, A. D. L., M. J. Miles, and J. K. Hobbs (2005). A mechanical microscope: High-speed atomic force microscopy. *Applied Physics Letters 86*(3), 034106.

Hyvamaki, T. (2008). Analysis of pid control design methods for a heated airfow process. *Independent research projects in applied mathematics*.

Kasas, S., N. H. Thomson, B. L. Smith, H. G. Hansma, X. Zhu, M. Guthold, C. Bus-

tamante, E. T. Kool, M. Kashlev, and P. K. Hansma (1997). Escherichia coli rna polymerase activity observed using atomic force microscopy. *Biochemistry 36*(3), 461–468.

Kodera, N., D. Yamamoto, R. Ishikawa, and T. Ando (2010). Video imaging of walking myosin v by high-speed atomic force microscopy. *Nature 468*, 72–77.

Kokavecz, J. and A. Mechler (2008). Spring constant of microcantilevers in fundamental and higher eigenmodes. *Phys. Rev. B 78*.

Lee, W., M. Balantekin, A. G. Onaran, W. L. Hughes, B. A. Buchine, R. O. Guldiken, Z. Parlak, C. F. Quate, and F. L. Degertekin (2006). A new atomic force microscope probe with force sensing integrated readout and active tip. *Review of Scientific Instruments 77*.

Liu, Y., Y. Qiao, D. Luo, Y. Min, T. Zhang, X. Cao, and Y. Zhou (2017). A precisely assembled carbon source to synthesize fluorescent carbon quantum dots for sensing probes and bioimaging agents. *Chemistry-A European Journal 24*(32).

Mahapatra, S. and B. Subudhi (2017). Design of a steering control law for an autonomous underwater vehicle using nonlinear h-infinity state feedback technique. *Nonlinear Dynamics 90*, 837 – 854.

Nair, S. S. (2011). Automatic weight selection algorithm for designing h infinity controller for active magnetic bearing. *International Journal of Engineering Science and Technology (IJEST) 3*(1).

Nakakuki, T., M. Ogawa, and C. Ishii (2012). Nonlinear robust stage control of atomic force microscope. *IEEE International Conference on Control Applications (CCA)*.

Oubellil, R., A. Voda, M. Boudaoud, and S. Regnier (2016). A 2-dof h-infinity control strategy for a 3 axes robotic system operating at the nanometer scale. In *20th International Conference on System Theory, Control and Computing (ICSTCC)*, pp. 355–362.

Peng, C., C. Han, J. Zou, and G. Zhang (2015). H infinity optimal inversion feedforward and robust feedback based 2dof control approach for high speed-precision

positioning systems. *Journal of Control Science and Engineering 2016*, 7256039.

quora.com (2018). https://www.quora.com/how-does-atomic-force-microscopy-work. *(Accessed: July 7, 2018)*.

Ramsdell, D. and K. Gaskell (2013). Afm standard operating procedure. *Surface Analysis Centre*.

Rigatos, G., P. Siano, M. Abbaszadeh, and S. Ademi (2017). Nonlinear h-infinity control for the rotary pendulum. In *11th International Workshop on Robot Motion and Control*, pp. 217–222.

Rigatos, G., P. Siano, P. Wira, and F. Profumo (2015). Nonlinear h-infinity feedback control for asynchronous motors of electric trains. *Intell Ind. Syst. 1*, 85–98.

Ryba, L. (2006). *3D Nanopositioning Based on Tunneling Current Measurement and Piezo Actuation*. Ph. D. thesis, GIPSA-Lab, Universite Grenoble Alpes.

Schafer, T. E. and C. Braunsmann (2010). High-speed atomic force microscopy for large scan sizes using small cantilevers. *Nanotechnology 21*(22), 225705.

Schitter, G., P. Menold, H. F. Knapp, F. Allgower, and A. Stemmer (2001). High performance feedback for fast scanning atomic force microscopes. *Review of Scientific Instruments 72*(8).

Schitter, G., R. Stark, and A. Stemmer (2004). Fast contact-mode atomic force microscopy on biological specimen by model-based control. *Ultramicroscopy 100*(3), 253–257.

Skogestad, S. and I. Postletwaite (1996). *Multivariable Feedback Control: Analysis and Design* (1st ed.). Wiley.

Sulchek, T., G. G. Yaralioglu, C. F. Quate, and S. C. Minne (2002). Characterization and optimization of scan speed for tapping-mode atomic force microscopy. *Review of Scientific Instruments 73*(8).

Uchihashi, T., N. Kodera, and T. Ando (2012). Guide to video recording of struc-

ture dynamics and dynamic processes of proteins by high-speed atomic force microscopy. *Nature Protocols 7*(6).

Viani, M. B., T. E. Schaffer, A. Chand, M. Rief, H. E. Gaub, and P. K. Hansma (1999). Small cantilevers for force spectroscopy of single molecules. *Journal of Applied Physics 86*(4), 2258–2262.

Wang, Y., X. Hu, and L. Xu (2016). An intelligent control scheme for precise tip-motion control in atomic force microscopy. *Scanning 138*, 93–99.

Wang, Y., J. Wan, X. Hu, L. Xu, and S. Wu (2015). A rate adaptive control method for improving the imaging speed of atomic force microscopy. *Ultramicroscopy 155*, 49–54.

Zhang, Q., R. Turton, and D. Bhattacharyya (2018). Nonlinear model predictive control and h-infinity robust control for a postcombustion co2 capture process. *International Journal of Greenhouse Gas Control 70*, 105–116.

Zhang, Y., Y. Li, G. Shan, Y. Chen, Z. Wang, and J. Qian (2018). Real-time scan speed control of the atomic force microscopy for reducing imaging time based on sample topography. *Micron 106*, 1–6.

Ziegler, J. G. and N. B. Nichols (1942). Optimum settings for automatic controllers. *Transactions of the A.S.M.E.*, 759–765.